



**COMPUTATIONAL FLUID DYNAMICS
TESTING FOR DRAG REDUCTION OF AN
AIRCRAFT LASER TURRET**

THESIS

Gregory J. Schwabacher, Captain, USAF

20000803 148

AFIT/GAE/ENY/00M-11

**DEPARTMENT OF THE AIR FORCE
AIR UNIVERSITY**

AIR FORCE INSTITUTE OF TECHNOLOGY

Wright-Patterson Air Force Base, Ohio

APPROVED FOR PUBLIC RELEASE; DISTRIBUTION UNLIMITED.

DTIC QUALITY INSPECTED 4

AFIT/GAE/ENY/00M-11

**COMPUTATIONAL FLUID DYNAMICS
TESTING FOR DRAG REDUCTION OF AN
AIRCRAFT LASER TURRET**

THESIS

**Gregory J. Schwabacher
Captain, USAF**

AFIT/GAE/ENY/00M-11

Approved for public release; distribution unlimited

Disclaimer

The views expressed in this thesis are those of the author and do not reflect the official policy or position of the United States Air Force, the Department of Defense, or the United States Government.

COMPUTATIONAL FLUID DYNAMICS TESTING FOR DRAG REDUCTION OF AN AIRCRAFT LASER TURRET

THESIS

Presented to the Faculty of the Graduate School of Engineering and Management
of the Air Force Institute of Technology
Air University
Air Education and Training Command
in Partial Fulfillment of the Requirements for the
Degree of Master of Science in Aeronautical Engineering

Gregory J. Schwabacher
Captain, USAF


March 2000

COMPUTATIONAL FLUID DYNAMICS TESTING FOR DRAG REDUCTION OF AN AIRCRAFT LASER TURRET

Gregory J. Schwabacher


Captain, USAF

Approved:



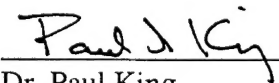
Major Jeffrey Bons
Committee Chairman

3 Mar 00
Date



Dr. Milt Franke
Committee Member

2 Mar 00
Date



Dr. Paul King
Committee Member

3 Mar 00
Date

Acknowledgements

This study could not have taken place without the work and hard efforts of a number of people. First and foremost, I'd like to thank Major Jeffrey Bons. Without Major Bons' insight, wisdom, and grasp of "the big picture", this project may have never gotten off the ground. I am grateful to him for providing me the focus and direction that I needed to press on at those times I was ready to throw my hands up in despair. I also appreciate the efforts of Major Monty Hughson in suggesting this area of research to me and for giving me the background to undertake a project of this magnitude. Dr. Milt Franke was also instrumental in moving this study forward. He was always available, willing, and able to provide valuable guidance and a helpful hand when questions popped up. Finally, I'd like to express my heartfelt gratitude to my wife, Kelly, for putting up with all my mood swings, rants, raves, frustrations, and jubilant moments during the course of this study. She pulled me back down to earth when the going got tough and always helped me to keep the proper perspective. I can only hope that I might someday be able to provide the same level of assistance to someone in a similar situation as the above individuals have provided me.

Table of Contents

	Page
Approval Page.....	ii
Acknowledgements.....	iii
Table of Contents.....	iv
List of Figures.....	vii
List of Tables	xi
List of Symbols.....	xiii
Abstract.....	xvii
<u>Chapter 1</u> <u>Introduction</u>	1
1.1 Background.....	1
1.2 Previous Research.....	2
1.3 Alternatives to Traditional Experimental Analysis.....	3
1.4 Research Objective and Scope.....	6
<u>Chapter 2</u> <u>Theory</u>	8
2.1 Primary Drag Mechanisms on Bluff Bodies.....	8
2.2 Secondary Drag Mechanisms on Bluff Bodies.....	9
2.3 Strategy for Drag Reduction.....	10
<u>Chapter 3</u> <u>Computational Facilities and Hardware</u>	11
3.1 Computer Hardware and Software	11
3.2 Physical Models.....	11

<u>Chapter 4</u>	<u>Computational Fluid Dynamics Modeling Considerations</u>	14
4.1	Finite Difference and Finite Volume Methods.....	14
4.2	Laminar and Turbulent Models	16
4.2.1	Skin-friction Drag	17
4.2.2	Pressure Drag	18
4.2.3	Turbulence Models.....	19
4.3	Grid Generation	21
4.3.1	Solution Dependence on Grid	22
4.3.2	Structured Grids	24
4.3.3	Unstructured Grids	27
4.4	Two-Dimensional Versus Three-Dimensional Modeling	29
4.5	Steady-State Versus Time-Varying Solution Techniques	30
<u>Chapter 5</u>	<u>Numerical Simulation</u>	32
5.1	Axisymmetric Laminar Spheres	32
5.1.1	Model Geometries and Boundary Conditions.....	32
5.1.2	Grid Construction.....	35
5.1.3	Solver Initialization and Flow Solution	41
5.2	Axisymmetric Laminar Turret Models.....	43
5.2.1	Model Geometries and Boundary Conditions.....	43
5.2.2	Grid Construction.....	48
5.2.3	Solver Initialization and Flow Solution	54
5.3	Axisymmetric Turbulent Turret Models.....	54

<u>Chapter 6</u>	<u>Results and Discussion</u>	55
6.1	Definitions	55
6.2	Axisymmetric Laminar Turret Model Results.....	59
6.2.1	Comparison of Axisymmetric Laminar Sphere Results to Experimental Data.....	59
6.2.2	Effects of Aft-Mounted Fairings on Drag Reduction in a Laminar Flow Field	64
6.3	Axisymmetric Turbulent Turret Model Results	71
6.3.1	Comparison of Axisymmetric Turbulent Sphere Results to Experimental Data.....	71
6.3.2	Effects of Aft-Mounted Fairings on Drag Reduction in a Turbulent Flow Field	78
<u>Chapter 7</u>	<u>Conclusions and Recommendations</u>	87
	Bibliography.....	92
	Vita.....	93

List of Figures

	Page
Figure 1.1.	R/ILCT turret placement.....2
Figure 2.1.	Low pressure wake behind cylinder due to separation9
Figure 3.1	Turret model.....12
Figure 3.2	Small (foreground) and large fairings12
Figure 4.1	Laminar and turbulent path lines17
Figure 4.2	Laminar and turbulent velocity profiles.....18
Figure 4.3	Structured grid in the physical domain around a blunt body26
Figure 4.4	Structured grid in the computational domain with constant step sizes $\Delta\xi$ and $\Delta\eta$ for the blunt body problem26
Figure 5.1	Axisymmetric sphere model geometry, domain, and boundary conditions, 5.06 m wide x 2.53 m high.....35
Figure 5.2	Mesh 1 boundary layer grid37
Figure 5.3	Mesh 2 boundary layer grid38
Figure 5.4	Axisymmetric bottom boundary sections39
Figure 5.5	Mesh 1, axisymmetric sphere.....40
Figure 5.6	Mesh 2, axisymmetric sphere.....41
Figure 5.7	Location of spherical centerline of turret extended onto large fairing model.....45
Figure 5.8	Location of width measurements taken on large fairing model45

Figure 5.9	Axisymmetric model of small fairing/turret combination	46
Figure 5.10	Axisymmetric model of large fairing/turret combination	46
Figure 5.11	Axisymmetric model of optimized fairing/turret combination	48
Figure 5.12	Mesh 1, small fairing/turret combination boundary layer grid	50
Figure 5.13	Mesh 1, large fairing/turret combination boundary layer grid	50
Figure 5.14	Mesh 1, optimized fairing/turret combination boundary layer grid	51
Figure 5.15	Mesh 2, small fairing/turret combination boundary layer grid	51
Figure 5.16	Mesh 2, large fairing/turret combination boundary layer grid	51
Figure 5.17	Mesh 2, optimized fairing/turret combination boundary layer grid	51
Figure 5.18	Mesh 1, small fairing/turret combination	52
Figure 5.19	Mesh 1, large fairing/turret combination	52
Figure 5.20	Mesh 1, optimized fairing/turret combination	52
Figure 5.21	Mesh 2, small fairing/turret combination	53
Figure 5.22	Mesh 2, large fairing/turret combination	53
Figure 5.23	Mesh 2, optimized fairing/turret combination	53
Figure 6.1	Pressure coefficient (axisymmetric sphere, laminar case) plots	60
Figure 6.2	Skin friction coefficient (axisymmetric sphere, laminar case) plots	61
Figure 6.3	Skin friction coefficient (axisymmetric Mesh 1 grids, laminar case) plots	64

Figure 6.4	Skin friction coefficient (axisymmetric Mesh 2 grids, laminar case) plots65
Figure 6.5	Mesh 2 axisymmetric clean sphere model separated region velocity vector plot66
Figure 6.6	Mesh 2 axisymmetric small fairing/turret combination model separated region velocity vector plot67
Figure 6.7	Mesh 2 axisymmetric large fairing/turret combination model separated region velocity vector plot67
Figure 6.8	Mesh 2 axisymmetric optimized fairing/turret combination model separated region velocity vector plot68
Figure 6.9	Pressure coefficient (axisymmetric Mesh 1 grids, laminar case) plots69
Figure 6.10	Pressure coefficient (axisymmetric Mesh 2 grids, laminar case) plots69
Figure 6.11	Boundary layer separation region associated with laminar axisymmetric optimized fairing/turret combination model.....71
Figure 6.12	Pressure coefficient (axisymmetric sphere, turbulent case) plots.....72
Figure 6.13	Skin friction coefficient (axisymmetric sphere, turbulent case) plots73
Figure 6.14	Skin friction coefficient (axisymmetric Mesh 1 grids, turbulent case) plots78

Figure 6.15	Skin friction coefficient (axisymmetric Mesh 2 grids, turbulent case) plots79
Figure 6.16	Mesh 2 axisymmetric turbulent clean sphere model separated region velocity vector plot80
Figure 6.17	Mesh 2 axisymmetric turbulent small fairing/turret combination model separated region velocity vector plot81
Figure 6.18	Mesh 2 axisymmetric turbulent large fairing/turret combination model separated region velocity vector plot81
Figure 6.19	Mesh 1 axisymmetric turbulent optimized fairing/turret combination model separated region velocity vector plot82
Figure 6.20	Pressure coefficient (axisymmetric Mesh 1 grids, turbulent case) plots.....84
Figure 6.21	Pressure coefficient (axisymmetric Mesh 2 grids, turbulent case) plots.....84
Figure 6.22	Pressure coefficient (axisymmetric small fairing/turret combo, turbulent case) plots.....86
Figure 6.23	Pressure coefficient (axisymmetric large fairing/turret combo, turbulent case) plots.....86

List of Tables

	Page
Table 5.1	Boundary layer parameters of axisymmetric sphere grids.....37
Table 5.2	Axisymmetric sphere boundary node spacing distributions39
Table 5.3	Axial and radial coordinates of small axisymmetric fairing numerical model.....46
Table 5.4	Axial and radial coordinates of large axisymmetric fairing numerical model.....46
Table 5.5	Axial and radial coordinates of optimized fairing numerical model.....48
Table 5.6	Boundary node distributions on axisymmetric turret/fairing grids.....50
Table 6.1	Percent difference in minimum computed pressure coefficient for axisymmetric laminar sphere cases versus Achenbach (1972).....60
Table 6.2	Percent difference in maximum computed skin friction coefficient for axisymmetric laminar sphere cases versus Achenbach (1972).....61
Table 6.3	Separation points in degrees and difference percentages for axisymmetric laminar sphere cases.....62

Table 6.4	Drag coefficients and difference percentages for axisymmetric laminar sphere cases.....	63
Table 6.5	Separation points in degrees for all axisymmetric laminar grids.....	65
Table 6.6	Drag coefficients for axisymmetric laminar turret/fairing combination models	70
Table 6.7	Drag reduction percentages for axisymmetric laminar turret/ fairing combination models compared to clean turret model	70
Table 6.8	Percent difference in minimum computer pressure coefficient for axisymmetric turbulent sphere cases versus Achenbach (1972).....	72
Table 6.9	Percent difference in maximum computed skin friction coefficient for axisymmetric turbulent sphere cases versus Achenbach (1972).....	74
Table 6.10	Separation points in degrees and difference percentages for axisymmetric turbulent sphere cases.....	75
Table 6.11	Drag coefficients and difference percentages for axisymmetric turbulent sphere cases.....	76
Table 6.12	Separation points in degrees for all axisymmetric turbulent grids.....	79
Table 6.13	Numerical and experimental drag coefficients and drag reduction percentages for all turret/fairing combinations	83

List of Symbols

<u>Symbol</u>	<u>Definition</u>
2D	two-dimensional
3D	three-dimensional
\vec{A}	surface area vector
A_f	magnitude of area of face f
ABL	Airborne Laser
AFB	Air Force Base
AFIT	Air Force Institute of Technology
AFRL/SN	Air Force Research Laboratory, Sensors Directorate
$C_{D_{calc}}$	calculated drag coefficient
$C_{D_{ref}}$	reference drag coefficient
C_f	skin friction coefficient
$C_{f_{max,ref}}$	maximum reference skin friction coefficient
$C_{f_{max,calc}}$	maximum calculated skin friction coefficient
$C_{f_{min,ref}}$	minimum reference skin friction coefficient
C_p	pressure coefficient
$C_{p_{max,ref}}$	maximum reference pressure coefficient
$C_{p_{min}}$	minimum pressure coefficient
$C_{p_{min,calc}}$	minimum calculated pressure coefficient

$C_{p_{min,ref}}$	minimum reference pressure coefficient
CFD	computational fluid dynamics
d	derivative operator
D	drag force <i>or</i> total derivative operator
D_{turret}	turret diameter
DEC	Digital Equipment Corporation
i	Cartesian direction
\hat{i}	unit vector in x-direction
\hat{j}	unit vector in y-direction
k	turbulent kinetic energy
MHz	megahertz
N_{faces}	number of faces enclosing cell
p	pressure
p_{gauge}	gauge pressure
p_{ref}	reference pressure
PDE	partial differential equation
$r_{optimized}$	optimized fairing radial coordinate
r_{turret}	turret radius
RAM	random-access memory
RANS	Reynolds-averaged Navier-Stokes
Re	Reynolds number
Re_D	Reynolds number (based on diameter)
R/ILCT	Reconnaissance/Intelligence Laser Communication Terminal

S	frontal area
S_ϕ	source of ϕ per unit volume
S-A	Spalart-Allmaras
t	time
u	magnitude of unit vector in x-direction
u_i	velocity component in i direction
u_i'	instantaneous velocity component in i direction
$\overline{u_i}$	mean velocity component in i direction
v	magnitude of unit vector in y-direction
V	cell volume
V_{ref}	reference velocity
\vec{v}	velocity vector
\vec{v}_f	mass flux through face
x	abscissal coordinate in Cartesian plane
x_i	spatial coordinate in i direction
y	ordinal coordinate in Cartesian plane

δ_{ij}	Kronecker delta
$\vec{\nabla}$	gradient
$(\vec{\nabla}\phi)_n$	magnitude of $\vec{\nabla}\phi$ normal to face f
$\Delta\eta$	step size in η -direction

$\Delta\xi$	step size in ξ -direction
ε	turbulence dissipation rate
ϕ	arbitrary scalar quantity <i>or</i> angle from leading edge of turret
ϕ'	instantaneous scalar quantity ϕ
$\overline{\phi}$	mean scalar quantity ϕ
ϕ_{calc}	calculated separation angle
ϕ_{ref}	reference separation angle
ϕ_f	value of ϕ convected through face f
Γ_ϕ	diffusion coefficient for ϕ
η	abscissal coordinate in computational plane
μ	viscosity
μ_{ref}	reference viscosity
μ_t	turbulent viscosity
π	pi
ρ	density
ρ_{ref}	reference density
τ_{wall}	wall shear stress
ξ	ordinal coordinate in computational plane
\int	integral operator
\oint	closed-surface integral operator

Abstract

A computational study was conducted on the use of aft-mounted fairings for passive drag reduction on a sphere at $Re_D=8.66 \times 10^5$. The sphere dimensions and operating Reynolds number were selected to approximate (in two dimensions) the flow around a proposed aircraft laser turret for which experimental data was available. To establish the validity of the computational model, flow predictions were compared to sphere data available in the open literature. The model, exercised in both the laminar and turbulent modes, showed good agreement with the published data. Two proposed laser turret fairings were then evaluated computationally: a large fairing (beginning at 49.5 degrees past the sphere apex) and a small fairing (beginning at 58.95 degrees past the sphere apex). Existing wind tunnel models were used to generate axisymmetric computational grids that approximated the geometry of these models. The computed flow field and associated drag reduction were comparable to the experimental results obtained from the wind tunnel testing. Differences in the C_D reduction from the model to the experiment were explained by the axisymmetric simplifications made in the model. Finally, a new, optimized fairing model was designed which completely eliminated the separation zone on the aft portion of the sphere. The optimized model predicted double the drag reduction compared to the large fairing computational model.

COMPUTATIONAL FLUID DYNAMICS TESTING FOR DRAG REDUCTION OF AN AIRCRAFT LASER TURRET

Chapter 1 – Introduction

1.1 Background

Historically, the development of airborne lasers has focused on their use as high-energy weapons systems capable of rapid deployment and pinpoint accuracy. Recently, however, strides have been made toward employing airborne lasers in a communications role. At the forefront of such efforts is the Air Force Research Laboratory Sensors Directorate (AFRL/SN) of Wright-Patterson Air Force Base. The directorate's Reconnaissance/Intelligence Laser Communication Terminal (R/ILCT) program aims to develop and demonstrate the feasibility of long-range, high-bandwidth laser communications between two high-altitude aircraft. Such a technology will provide the ability to transmit and receive reconnaissance and intelligence information from a forward location via a secure data link. The R/ILCT could also be used for communication between aircraft and ground stations, and future developments would permit communications with space-based platforms.

To demonstrate the ability of the R/ILCT to communicate between two aircraft, two decommissioned Air Force jets, T-39 Sabreliners, have been designated to test the R/ILCT. In order to house the R/ILCT's laser system, the exterior of the planes have been modified to include a 0.46 m diameter turret. The turret was placed underneath the

aircraft along its centerline and even with the wing root leading edge. Figure 1.1 shows the placement of the turret and a general layout of the R/ICLT system.

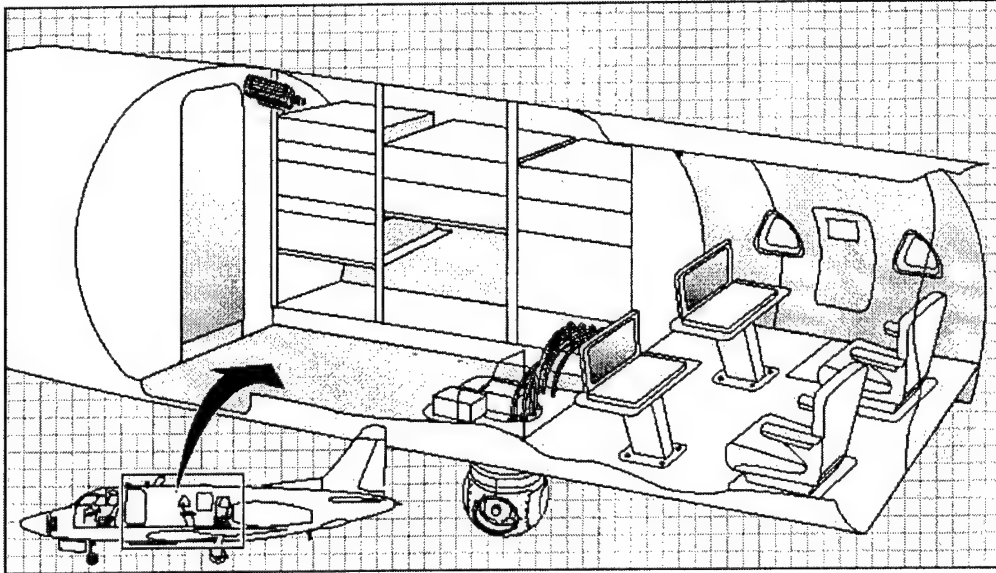


Figure 1.1. R/ILCT turret placement (Snyder, 1998: 2)

Clearly, a major design parameter facing any aircraft designer is drag reduction. Furthermore, a standard T-39 mission profile includes a large portion of flying time spent in the climb and descent phases. Placing a spherical R/ICLT turret on a T-39's fuselage exterior will incur a substantial drag penalty, further extending the amount of time consumed in the climb and descent phases. This will increase fuel consumption and reduce effective mission time at altitude. For these reasons, reducing the amount of drag induced by the turret modification becomes paramount.

1.2 Previous Research

In the mid-1970s, testing of geometries similar to that of the R/ICLT turret were carried out at Wright-Patterson AFB in support of the Airborne Laser Laboratory (ALL)

program. Emphasis was placed on drag reduction and force and vibration minimization, and many methods of drag reduction were employed, including boundary layer suction, mass flow injection, and the addition of aerodynamic shapes, such as scoops, channels, and fairings. The studies concluded that the lowest drag configuration consisted of the turret, a forward-ramped shell, and an aft fairing. This configuration reduced the baseline drag by 30% (Walterick and Van Kuren, 1975: 39).

Since significant differences existed between turret configurations studied earlier and the R/ICLT turret, further work was still necessary. In 1998, Snyder studied passive drag reduction of the R/ICLT through the use of aft-mounted splitter plates and fairings. Five configurations were tested in total on one-half scale models; the clean turret, the turret plus a large splitter plate, the turret plus a small splitter plate, the turret plus a large fairing, and the turret plus a small fairing. Snyder found that minimal drag reductions were realized through the use of splitter plates but that by using the small and large fairings, the baseline drag was reduced by 49% and 55%, respectively. The small fairing was unable to produce attached flow over the top of the turret, while the large fairing eliminated the majority of flow separation (Snyder, 1998: 70).

1.3 Alternatives to Traditional Experimental Analysis

Although traditional wind tunnel experimentation and analysis provides a viable means for observing, designing, and predicting the behavior of drag reduction devices, there are other methods available which are also valuable in aerodynamics research. Among such methods is computational fluid dynamics (CFD). The explosion of the

capabilities of the high-speed digital computer combined with the development of advanced numerical methods for solving physical problems on these computers has revolutionized the study of aerodynamics. Over the past 20 to 30 years, CFD has evolved to the point where today it is a widely used, and often preferred, design tool.

Computational fluid dynamics offers several marked advantages compared to traditional experimental methods of studying aerodynamic problems. First, CFD can be used to predict flow field behavior in flow regimes for which no wind tunnel is available; for example, no wind tunnels exist which can simultaneously simulate the higher Mach numbers and high flow field temperatures to be encountered by trans-atmospheric vehicles. CFD studies also allow the variation of Reynolds number over an almost infinite range; Reynolds number effects can be easily studied in numerical models whereas the limits in the operating envelope of wind tunnels may not permit this. Secondly, results achieved in numerical simulations are both highly accurate and infinitely repeatable and are not subject to measurement errors, device calibrations, and outside influences as are wind tunnel tests. Next, the costs of performing a CFD analysis are much lower than those associated with performing a similar wind tunnel experiment. Computer speed has increased at a much more rapid pace than computer cost – the net effect being an astounding decrease in the cost of performing a given computation. In fact, the cost of performing a given calculation has decreased by a factor of 10 every 8 years since about 1950 (Tannehill et al, 1995: 4). Conversely, the costs of performing a wind tunnel experiment have increased over the years – building models, calibrating equipment, providing power and consumables, and maintaining equipment – all are more

expensive than they used to be. Fourth, CFD analysis lends itself to easy model modification and optimization. In order to see the effects of a particular design change with a CFD model, all that is required is to simply modify the computer geometry of the model and re-run the numerical solver. The process is not so simple with experimentation. The wind tunnel must either be physically modified or completely rebuilt, then the physical experiment must be re-initialized and re-run – an especially time-consuming, expensive, and laborious procedure. Finally, and arguably most importantly, CFD can be used to provide an accurate description and visualization throughout the entire flow field of the problem being analyzed. This is extremely beneficial in understanding the underlying physics and associated flow field interactions that result in certain flight characteristics and behaviors. With wind tunnel experimentation, flow field measurements and visualizations are only available where data collection equipment has been placed. It is virtually impossible to predict the flow parameters at every point in the flow field simultaneously.

Unfortunately, there are drawbacks to computational fluid dynamics as well. First, it can be difficult to model extremely complex physics accurately in all situations with current numerical algorithms. Boundary layer transition and separation are two phenomena that can be particularly troublesome to predict with a high degree of accuracy. Second, many problems must be simplified to make them tractable. With some problems, the computer resources may not be available to solve the problem to the level of accuracy originally desired. Examples of problem simplification include modeling a three-dimensional problem as a two-dimensional or axisymmetric problem,

reducing the computational domain size or solution resolution of a given flow field, or modeling a time-varying problem as a steady-state problem. Third, certain assumptions must be made to obtain a solution. Usually these assumptions appear as boundary conditions and are relatively accurate – examples are asymptotic behavior at far-field boundaries or prescribed inlet or exit conditions. Fourth, a particular solution algorithm might not produce a converged solution for a given flow field. In many cases, simply using intuition and applying specifically suited algorithms to the problem at hand can avoid this problem.

An optimal way to use CFD is in conjunction with experimental studies. For example, initial computational models could be made which mimic past experimental models. These numerical results generated for these new models would then be used to validate the computer model against experimental findings. Once the numerical models have been validated, design optimization could be carried out on the computer. As soon as an optimized computer model has been completed, a physical twin of this model could be manufactured and tested experimentally. This method of using CFD and experimentation hand-in-hand provides the best of both worlds: enhanced accuracy, flow behavior prediction for any operating conditions, reduced expense, and reduced design time.

1.4 Research Objective and Scope

The goals accomplished by this study were threefold. First, solving the flow field around simple sphere geometries validated the computational fluid dynamics technique.

Pressure, skin friction, drag, and separation angle data were computed and compared to published experimental results. Second, CFD models were created to match Snyder's experimental fairing geometries and solutions were obtained for the flow field around two numerical turret/fairing models. These results (pressure coefficient, drag coefficient, and separation angle) were compared to Snyder's experimental data. Additionally, the percentage of drag reduction for each fairing compared to the clean turret was computed and compared to Snyder's findings. Finally, a third optimized CFD fairing/turret combination was modeled about which the flow field was computed. The associated pressure coefficient, separation angle, and drag coefficient results were compared to the other CFD results, demonstrating the feasibility and ease of using this approach for fairing design optimization. Conditions matching those prevalent in Snyder's study were used for all computational models; namely, the flow inlet velocity was set to 55 m/s such that the flow Reynolds number (based on turret diameter) was 8.66×10^5 .

Chapter 2 – Theory

2.1 Primary Drag Mechanisms on Bluff Bodies

This study primarily focused on the drag force produced by airflow about one fundamental bluff body shape – the sphere, with and without aft fairings. The total drag on a body is defined as the component of the aerodynamic force acting on that body parallel to the freestream velocity. It is comprised of three components: skin friction drag, pressure drag, and induced drag due to lift. Since the bodies studied were symmetrical about the horizontal plane, the net lift force was zero, therefore, the remaining constituents of the drag force were skin friction and pressure forces.

Skin friction drag is the result of shear stresses acting tangential to the surface of the body. Conversely, pressure drag is the result of pressure forces acting normal to the surface of the body. In the case of bluff bodies, pressure drag forces are usually many times higher than skin friction forces. In this study, the primary cause of pressure drag was boundary layer separation and the resulting wake (Figure 2.1) that formed aft of the body. Flow separation occurs when flow attached to the body encounters an adverse pressure gradient. If the pressure gradient is severe enough, the flow will detach from the body, generating a turbulent wake. Due to its lower pressure compared to flow near the front of the body, this wake produces a large pressure differential, and thus a substantial drag force. The size of this wake, which is determined by the boundary layer separation point, has a proportional influence on the amount of pressure drag – the smaller the wake, the lower the pressure drag. Turbulent boundary layers, due to their higher turbulent

kinetic energy relative to laminar boundary layers, tend to resist the effects of adverse pressure gradients and separate farther downstream. Thus, the pressure drag associated with turbulent flows tends to be significantly lower than the pressure drag associated with laminar flows.

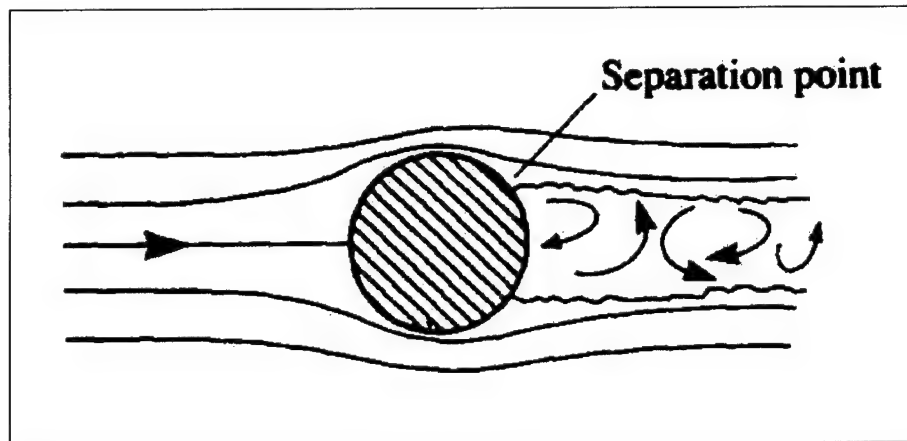


Figure 2.1. Low pressure wake behind cylinder due to separation

2.2 Secondary Drag Mechanisms on Bluff Bodies

Vortex shedding is also an important phenomenon associated with flows over bluff bodies. In the wake of two-dimensional bodies, such as cylinders, a relatively stable system called a vortex street is formed. The two sides of the 2D cylinder alternate periodically in releasing a straight vortex which swirls about an axis parallel to the cylinder's axis; the resulting street moves up and down and a regular flow pattern is established. As flow Reynolds number increases, the vortex pattern becomes less ordered; eventually, a clear vortex pattern disappears and is replaced with a chaotic turbulent wake. Vortex systems about three-dimensional bodies have the potential of forming about multiple axes of rotation, interacting unpredictably and creating an extremely complex flow field. In both 2D and 3D bluff body cases, the interaction of the

wake vortices increases the zone of vorticity aft of the body and augments the strength of the low-pressure wake behind the body, thereby increasing drag. However, due to limitations that will be discussed later and the fact that Snyder's attempts to reduce vortex interaction by employing splitter plates were shown to have a negligible effect on drag reduction (Snyder, 1998: 70), vortex streets were not modeled or studied in this research.

2.3 Strategy for Drag Reduction

The strategy for reducing pressure drag considered in this study was through the use of passive devices, called fairings, designed to delay or prevent separation of airflow around the bluff body. If boundary layer separation is delayed or eliminated, the size of the low-pressure wake behind the body is reduced, effectively lowering pressure drag on the body. In addition, even if separation does occur, fairings can provide a streamlined shape to which the detached flow can reattach, thereby creating a means to minimize the size and strength of the low pressure wake.

Chapter 3 – Computational Facilities and Hardware

3.1 Computer Hardware and Software

All computational modeling and testing was performed in the AFIT Aerodynamics Computational Laboratory. For this study, a 433 MHz DEC Alpha workstation with 256 megabytes of RAM running Digital UNIX/Common Desktop Environment V1.0 was used. This workstation is equipped with two commercial software packages tailored for CFD analysis: GAMBIT I, the grid generator, and FLUENT 5, the numerical solver. FLUENT 5 is a state-of-the-art computer program for modeling fluid flow and heat transfer in complex geometries. It provides complete mesh flexibility for solving flow problems with unstructured meshes that can be generated about complex geometries with relative ease.

3.2 Physical Models

The computational models used in this project were derived from the turret model and small and large fairings used in Snyder's experimental work (Figures 3.1-3.2). The turret diameter is 0.23 m, and each fairing is the same length of approximately 64 cm.



Figure 3.1. Turret model (Snyder, 1998: 12)

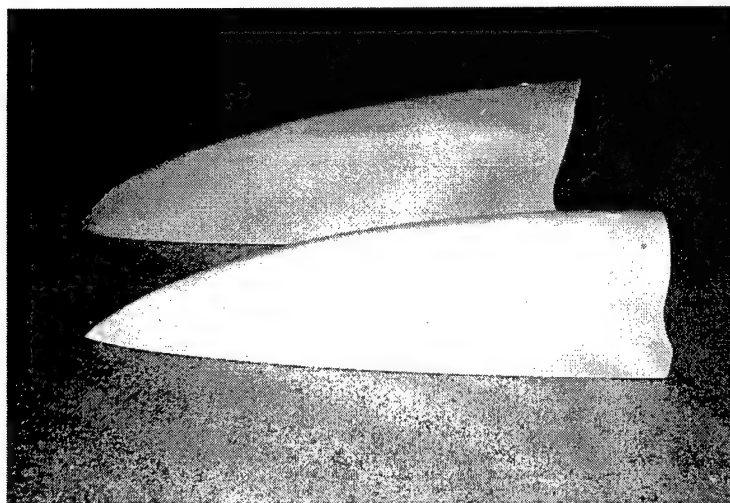


Figure 3.2. Small (foreground) and large fairings

The maximum look angle available to the laser system is an important consideration in the design of any drag reduction device placed on the turret. The look

angle is defined as the maximum angle to which the turret can rotate to either side of center while maintaining an unobstructed view through the 60 degree laser viewing window (Snyder, 1998: 16). Because of the size of the viewing window, any modification to the turret must not obstruct an area larger than the desired maximum look angle plus 30 degrees. The small and large physical fairings modeled in this project allow maximum look angles of 120 degrees and 90 degrees, respectively.

Chapter 4 – Computational Fluid Dynamics Modeling Considerations

4.1 Finite Difference and Finite Volume Methods

All of computational fluid dynamics, in one form or another, is based on the governing equations of fluid dynamics: the continuity, energy, and momentum equations. These equations mathematically state three things, respectively; that mass is conserved, that energy is conserved, and that force equals mass times acceleration. In general, these governing equations can be written in two forms: the integral form and the partial differential equation, or PDE, form. Though the form of the equations makes little difference with regard to aerodynamic theory, these different equation forms lead to vastly different CFD solution algorithms.

Since computers are unable to directly solve the governing equations of fluid motion, these equations must be transformed into forms that computers can handle; namely, the partial derivatives (or integrals) in the equations must be replaced with discrete numbers. In short, the continuous problem domain is discretized so that the dependent variables are computed only at discrete points. Derivatives and integrals are approximated by differences, which lead to an algebraic representation of the governing equations. In this way, a calculus problem is effectively transformed into an algebraic problem. Discretization of the PDE form of the governing physical equations leads to *finite differences*, whereas discretization of the integral form of the governing physical equations leads to *finite volumes*.

FLUENT uses a finite volume-based algorithm to transform the governing physical equations to algebraic equations that can be solved numerically. In such an approach, the computational domain is subdivided into individual, discrete control volumes, or cells. The governing equations about each cell are then integrated, yielding discrete equations that conserve each quantity on a control-volume basis (Fluent Inc., 1998: 17-9).

Consider the following steady-state conservation equation for transport of a scalar quantity ϕ written in integral form for an arbitrary control volume V (Fluent Inc., 1998: 17-9):

$$\oint \rho \phi \vec{v} \cdot d\vec{A} = \oint \Gamma_{\phi} \vec{\nabla} \phi \cdot d\vec{A} + \int_V S_{\phi} dV$$

where

$$\begin{aligned} \rho &= \text{density} \\ \vec{v} &= \text{velocity vector } (= u\hat{i} + v\hat{j} \text{ in 2D}) \\ \vec{A} &= \text{surface area vector} \\ \Gamma_{\phi} &= \text{diffusion coefficient for } \phi \\ \vec{\nabla} &= \text{gradient of } \phi \\ S_{\phi} &= \text{source of } \phi \text{ per unit volume} \end{aligned}$$

This equation is applied to each cell in the computational domain. FLUENT discretizes this integral equation as

$$\sum_f^{N_{\text{faces}}} v_f \phi_f A_f = \sum_f^{N_{\text{faces}}} \Gamma_{\phi} (\vec{\nabla} \phi)_n A_f + S_{\phi} V$$

where

$$\begin{aligned}
N_{\text{faces}} &= \text{number of faces enclosing cell} \\
\phi_f &= \text{value of } \phi \text{ convected through face } f \\
\overrightarrow{v_f} &= \text{mass flux through the face} \\
A_f &= \text{area of face } f, |A| \\
(\overrightarrow{\nabla\phi})_n &= \text{magnitude of } \overrightarrow{\nabla\phi} \text{ normal to face } f \\
V &= \text{cell volume}
\end{aligned}$$

The equations solved by FLUENT that lead to a full description of the flow field around a given object take the same form as the discretized equation above and apply to multi-dimensional, unstructured meshes comprised of arbitrarily-shaped polyhedra (Fluent Inc., 1998: 17-10).

4.2 Laminar and Turbulent Models

Since experimental results were available in the open literature for both laminar and turbulent flow over spheres, it was necessary to demonstrate the validity of the computational flow solver over a full range of flow conditions by employing both laminar and turbulent computational models. Further, since the data from Snyder's experiments was taken over a range of Reynolds numbers where the flow was expected to undergo a transition from laminar to turbulent, accurate laminar and turbulent numerical flow predictions were necessary to effectively compute the effects of the passive drag reduction devices on the laser turret.

In general, viscous flow over a surface can be characterized in two ways. If the path lines of the various fluid elements that make up the flow move smoothly and evenly, as shown on the left in Figure 4.1, then the flow is called laminar. Conversely, if the movement of the fluid elements is rough and erratic, as shown on the right in Figure 4.1,

then the flow is called turbulent. The characterization of the flow field is particularly important in this study because laminar and turbulent flow fields contribute very differently to the total drag on a given body.

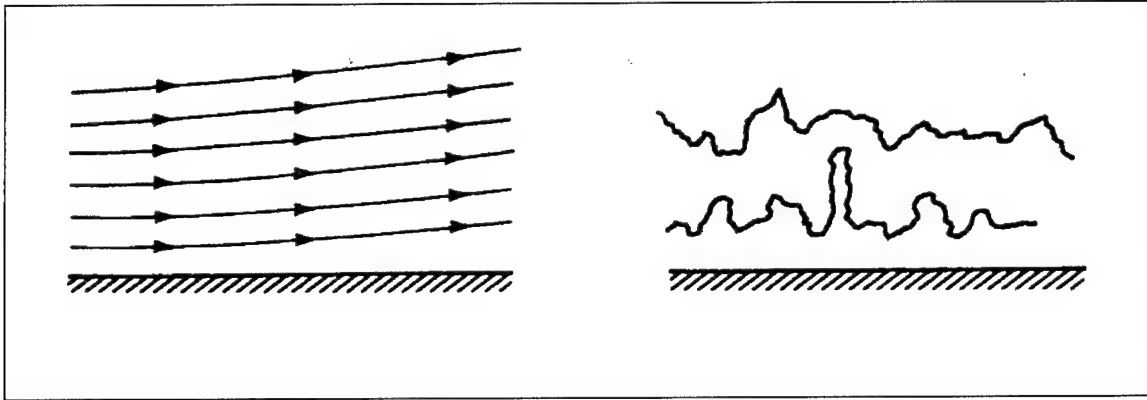


Figure 4.1. Laminar and turbulent path lines

4.2.1 Skin-friction Drag

Due to the irregular motion of the fluid elements in a turbulent flow field, elements with higher kinetic energy from the outer regions of the flow are readily circulated close to the surface of the body. Thus, the average flow velocity near the body surface is larger for a turbulent flow than for a comparable laminar flow. This phenomenon is demonstrated in Figure 4.2, which shows the relative velocity profiles for laminar and turbulent flow.

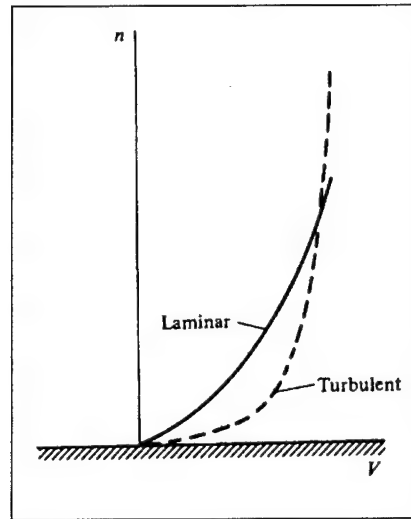


Figure 4.2. Laminar and turbulent velocity profiles

Directly above the surface, the slope of the turbulent velocity profile is much greater than the laminar curve's slope. Since the shear stress (and skin friction force) on the body is directly proportional to the velocity gradient at the surface, it is clear that the skin friction drag is larger for the turbulent flow in comparison with the laminar flow.

4.2.2 Pressure Drag

Although turbulent flows demonstrate higher skin friction drag values than comparable laminar flows, this trend does not continue when it comes to pressure drag. In fact, much the opposite takes place. Because of their higher kinetic energy, turbulent flows are better able to resist the effects of adverse pressure gradients that are encountered as the flow passes around a body. Therefore, turbulent flows are less likely to separate from the body surface. If flow separation happens to occur, the resulting wake will be much smaller. Since there is a smaller turbulent wake, the pressure drag associated with this wake will also be lower.

4.2.3 Turbulence Models

Turbulent flows are primarily characterized by fluctuating velocity fields. Because these fields transport momentum, energy, and other quantities, the fields cause the transported quantities to fluctuate as well. Since these fluctuations are often high in frequency and small in scale, they are simply too computationally expensive to directly simulate for the vast majority of engineering problems. Instead, the governing fluid dynamics equations are manipulated to remove the small-scale effects while still capturing the bulk turbulent effects. Though these new equations are more computationally efficient, they also introduce new unknown variables, and turbulence models are needed to determine these values in terms of known quantities.

Several turbulence models are prevalent today. Each model is tailored to a specific type of flow, and unfortunately, there does not exist one single model that is equally well-suited for all types of problems. Selection of an appropriate turbulence model for a particular problem depends on many factors; among them are the physics present in the flow, the level of accuracy desired, the available computational resources, and the amount of time available for the simulation.

One particular class of turbulence models (that includes the Spalart-Allamas and $k-\varepsilon$ models, among others) generally adopted for practical engineering calculations is based on the Reynolds-averaged Navier-Stokes equations. As mentioned earlier, in

Reynolds averaging, the solution variables in the exact Navier-Stokes equations are decomposed into the mean and fluctuating components. For velocity, this leads to

$$u_i = \bar{u}_i + u'_i$$

where

$$\begin{aligned}\bar{u}_i &= \text{mean velocity component } (i = 1, 2, 3) \\ u'_i &= \text{instantaneous velocity component } (i = 1, 2, 3)\end{aligned}$$

Likewise, for other scalar quantities ϕ (such as pressure or energy), the relationship is

$$\phi = \bar{\phi} + \phi'$$

Substituting expressions of this form into the exact Navier-Stokes continuity and momentum equations and taking a time average leads to the Reynolds-averaged Navier-Stokes (RANS):

$$\begin{aligned}\frac{\partial \rho}{\partial t} &= \frac{\partial}{\partial x_i}(\rho u_i) = 0 \\ \rho \frac{Du_i}{Dt} &= -\frac{\partial p}{\partial x_i} + \frac{\partial}{\partial x_j} \left[\mu \left(\frac{\partial u_i}{\partial x_j} + \frac{\partial u_j}{\partial x_i} - \frac{2}{3} \delta_{ij} \frac{\partial u_l}{\partial x_l} \right) \right] + \frac{\partial}{\partial x_j} (-\rho \overline{u'_i u'_j})\end{aligned}$$

These equations have the same general form as the exact Navier-Stokes equations. Additional terms, or Reynolds stresses $(-\rho \overline{u'_i u'_j})$, represent the effects of turbulence, and must be modeled in order to complete the equation set. A common approach, called the Boussinesq hypothesis, is to relate the Reynolds stresses to the mean velocity gradients:

$$-\rho \overline{u'_i u'_j} = \mu_t \left(\frac{\partial u_i}{\partial x_j} + \frac{\partial u_j}{\partial x_i} \right) - \frac{2}{3} \left(\rho k + \mu_t \frac{\partial u_l}{\partial x_l} \right) \delta_{ij}$$

The primary advantage to this method is that the computational cost associated with incorporating the turbulent viscosity into the solution algorithm is low. However, a drawback to this approach is that it assumes that μ_t , the turbulent viscosity, is an isotropic

scalar quantity, which is not strictly true. This hypothesis is used in the Spalart-Allmaras (S-A) model and the $k-\varepsilon$ turbulence models (Fluent Inc., 1998: 9-5).

The Spalart-Allmaras turbulence model that was used in this study is a simple one-equation model that solves a modeled transport equation for the turbulent viscosity. This model was designed for aerospace applications involving wall-bounded flows and has been gives good results for boundary layers subjected to adverse pressure gradients (Fluent Inc., 1998: 9-6), much like the flow fields encountered in this project. Although the original Spalart-Allmaras model requires that the viscous-affected region of the boundary layer be properly resolved through the use of a fine mesh inside the boundary layer, the model has been modified for its implementation in FLUENT so that wall functions are used when the mesh resolution is not sufficiently fine near object surfaces. The fact that the S-A model is a one-equation model with relatively lax grid density requirements further enhances its suitability for this particular study since, for the computer platform used, maximum computational efficiency was critical.

4.3 Grid Generation

Analytical solutions of fluid dynamics problems involve closed-form mathematical expressions that describe the variation of the dependent variables continuously throughout the problem domain. However, numerical solvers cannot generate closed-form analytical expressions, and instead calculate the dependent variables' values only at discrete points in the domain. These points are called grid points, or nodes. In order for a computational fluid dynamics software package to

provide a complete flow field description for a particular problem, the user must specify a grid that tells the flow solver at what locations in the problem domain the solution is to be computed. The specifics of the grid's construction can have a major influence on the fidelity of the solution and can, in fact, determine whether a solution is even attainable.

4.3.1 Solution Dependence on Grid

The quality and efficiency of the numerical solution is highly dependent on the construction of the grid used in the computational model. Several factors must be considered when generating a grid to ensure that the best possible numerical results are obtained with a particular solution algorithm.

Grid point placement can have a substantial effect on the stability and convergence of the numerical solver. For example, if grid points are not adequately concentrated in regions of high flow parameter gradients (such as near shock waves, in boundary layer separation regions, or near stagnation points), the numerical solver may not be able to adequately resolve these gradients in the flow field. Because obtaining the solution numerically is an iterative process, it is possible, and quite likely, that an insufficiently fine mesh will preclude the adequate calculation of important flow features, leading to oscillations in computed parameters or even divergence of the solution.

In numerical grid construction, there is an important trade-off between mesh density, solution efficiency, and solution accuracy. Generally, the more grid points contained in a given grid, the more accurate the final, converged solution will be.

However, the density of the grid cannot be arbitrarily increased without bound. Computer processor speed and memory limitations often dictate how fine a mesh can realistically be. Increasing the density of a mesh too much can quickly cause a given problem to become intractable. Along these same lines, it is important for the CFD analyst to carefully concentrate grid points in high-gradient regions while keeping the grid density throughout the majority of the computational domain fine enough for accuracy yet sparse enough for speed. Clearly, the maximum allowable grid point density of a particular simulation is highly dependent on the speed and capabilities of the computer platform being used.

In the case of unstructured grids (discussed in more detail later), solution accuracy, convergence, and efficiency are also highly dependent on the shape of the elements used to form the mesh. Two primary element shapes are used when generating unstructured grids: triangles and quadrilaterals. Due to fewer constraints on their use, grids constructed of triangular elements are often easier to build around complex geometries than are quadrilateral grids, especially when using an automatic grid generation program like GAMBIT. Element skewness also tends to be less of a factor with triangular element grids. Since the relative skewness of elements has a direct influence on the robustness of the numerical model, particularly in high-gradient regions, triangular element-based grids hold an advantage in this regard. However, the price one pays when using triangular elements is in efficiency. Since for a given node distribution there is a higher concentration of triangular elements than there would be of quadrilateral

elements, the use of triangular elements incurs a large speed penalty on the numerical solver.

Analysts must also take into account the size of the computational domain when modeling a CFD problem. Again, this is a situation where a trade-off is necessary. If the domain is large, boundary effects will not propagate into the problem's main region of interest and the solution will be free of adverse boundary/domain interactions. However, the problem can quickly become intractable if the domain is too large, and loss of efficiency becomes a serious issue. On the other hand, if the domain is small, the grid point distribution can be relatively dense while still keeping the problem tractable. However, if the domain is too small, the boundaries will interact adversely with the interior of the solution domain and inaccuracies in the solution will result.

4.3.2 Structured Grids

There are two types of grids commonly used in CFD research today – structured grids and unstructured grids. Naturally, each type has its own advantages and disadvantages, and these factors must be carefully weighed to determine which type of grid is best suited to a particular problem. Frequently, the *computational* domain of a given problem is selected to be rectangular in shape and its interior grid points are distributed at regularly-spaced intervals along grid lines. Since the grid points can be identified easily with their respective grid lines, such a grid is called a structured grid. Structured grids require a transformation from the physical space to the computational space. On the other hand, another type of grid system can be constructed where the grid

points cannot be directly associated with orderly, defined grid lines; though not random, the distribution of grid points cannot be predicted in a well-defined manner. This type of grid is called an unstructured grid (Hoffman and Chiang, 1998: 1-359).

Within a rectangular *physical* domain, the generation of a *computational* grid with uniform spacing is a relatively simple task. Unfortunately, the majority of physical domains of interest are not strictly rectangular in shape. Trying to impose a rectangular computational grid on a non-rectangular physical domain will require interpolation for the implementation of boundary conditions. This is not desired, since the boundary conditions have a major impact on the quality of the numerical solution. Further, complications in discretization at the edges of the computational domain make this approach less than ideal. In order to overcome these difficulties, a transformation from physical space to computational space is introduced that will map a non-rectangular coordinate system in the physical space (Figure 4.3) to a rectangular system in the computational space (Figure 4.4). To eliminate the discretization difficulties associated with non-equal step sizes in the computational domain, particularly for the finite-difference approach, *physical* domains are generally transformed into rectangular, constant step-size, *computational* domains. Also, it can be seen that deformation of the physical domain is usually necessary to obtain the computational domain.

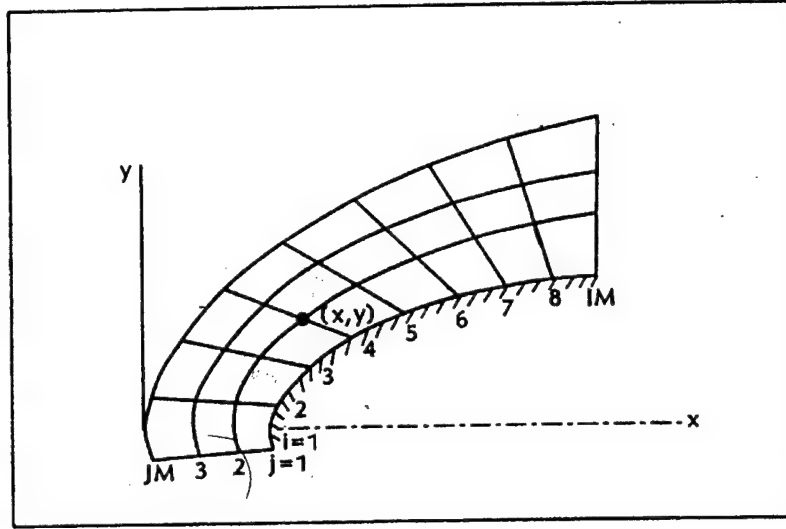


Figure 4.3. Structured grid in the physical domain around a blunt body

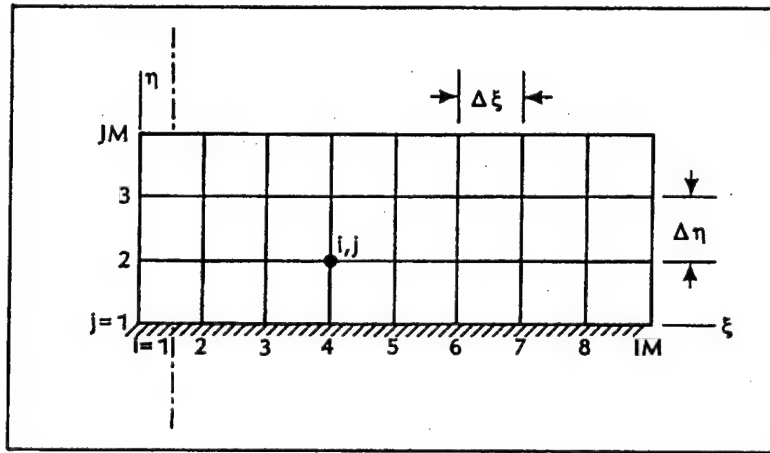


Figure 4.4. Structured grid in the computational domain with constant step sizes $\Delta\xi$ and $\Delta\eta$ for the blunt body problem

To determine the mapping of grid points in physical space to computational space, a few limitations are necessary. First, the mapping must be one-to-one; grid lines cannot cross one another. Second, a smooth grid point distribution, minimum grid line skewness, near-orthogonality, and concentration of grid points in regions of interest (i.e. high flow gradients or large dependent variable fluctuations) are all desired. There are

three primary structured grid generation techniques prevalent today: algebraic methods, partial differential methods, and conformal mappings based on complex variables. Each of these techniques involves solving a system of equations; given fixed step sizes in the computational domain, the solution of these equations provides the coordinates of the grid points in the physical domain. Modifying certain parameters within these equations allows the analyst to tailor the grid (to some degree) to provide higher grid resolution in physical areas of interest (boundary layers, separation regions, etc). Finally, the grid system may be either fixed or adaptive. A fixed system is generated prior to the solution of the governing equations and does not change as a result of the solution, where an adaptive grid system morphs as a result of the solution (for example, grid points may become concentrated in regions of high gradients, such as in the neighborhood of a shock wave).

4.3.3 Unstructured Grids

It is interesting to note that discretization of a domain can be accomplished either directly in the physical space or in the transformed computational space; the choice depends mainly on the numerical solution method and the domain of the solution. For those solution schemes (such as the finite volume method that FLUENT employs) where the governing fluid dynamics equations are integrated numerically on the physical domain and solved, the corresponding grid system is usually generated directly in the physical domain. In such cases, the domain of solution is divided into individual cells (usually triangles or quadrilaterals in 2D or pyramids or tetrahedrons in 3D) and for these cases, the grid points generally cannot be associated with grid lines. Instead, the points'

locations must be individually specified. This type of grid system is known as an unstructured grid.

Besides being a natural choice for use with finite volume numerical solvers, there are also a number of advantages that unstructured grids enjoy over structured grids. The main advantage of an unstructured grid is that it can be used with equal ease and success over a wide variety of surface geometries. Unstructured grids can also be used for both irregular, singly-connected domains as well as multiply-connected domains. Since unstructured grids do not rely on a mathematical transformation, or mapping, from physical space to computational space, they lend themselves more readily to node placement optimization. In other words, it is much easier to arbitrarily concentrate points in regions in the domain of high interest; for example, near large pressure gradients, inside boundary layers, or around shocks. By the same token, unstructured grids are also more easily coupled with grid refinement techniques for automated grid adaptation. However, unstructured grids have their drawbacks as well. Since the position of each node is not determined by the solution to a set of equations, but instead, is defined explicitly, there is a substantial amount of bookkeeping associated with defining the position of every node in the unstructured mesh. This added data manifests itself in increased program complexity and reduced computational efficiency of CFD solutions of problems using unstructured grids compared to structured grids.

4.4 Two-Dimensional Versus Three-Dimensional Modeling

Since most physical flows are three-dimensional, it seems logical that a three-dimensional model would be the ideal choice for solving most real-world problems. However, in those real flows where the salient features are primarily two-dimensional or axisymmetric in nature (for example, flow over a high aspect ratio wing or flow around a sphere, respectively), two-dimensional computational models often provide a sufficiently accurate description of the major flow features to render the inclusion of the third dimension unnecessary. In fact, the additional computational load incurred by modeling and solving a full three-dimensional flow field can be substantial; increases in solution time on the order of ten or more are common – an estimate of the difference between 2D and 3D computational workloads is provided in Section 5.1.1. Two-dimensional solutions are, of course, unable to resolve complex three-dimensional flow features (like 3D vortex interactions), but in those cases where the physical geometry warrants it, 2D models are often preferred for the significant efficiency advantages they provide. In addition, the sophistication of grids required for two-dimensional problems is greatly reduced compared to those required for full three-dimensional simulations. This has advantages both for the analyst and the grid generation software – the analyst can design a 2D computational mesh much more quickly than a 3D mesh, and the grid generation software (in this case, GAMBIT I), can compute the associated node distribution for a given mesh boundary spacing much more efficiently and with a greater degree of success for a 2D case than for a 3D case. Since GAMBIT has been shown to have difficulty generating quadrilateral element-based meshes for 2D geometries, adding a third

dimension would provide even more complexity and increase the likelihood of unstructured mesh generation problems.

4.5 Steady-State Versus Time-Varying Solution Techniques

The last major consideration to be made when solving a particular CFD problem is to decide whether to model the problem using a steady-state technique or a time-varying technique. Since all real-world problems take place over time, it seems natural to model problems as time-varying. However, there are several compelling reasons against this approach. First, if the bulk flow field parameters do not vary with time, and instead attain a steady-state condition, a steady-state technique is the obvious choice. Second, even if time-varying elements are present in the real flow, there may be good reason to model the flow using a steady-state approach, in which case the analyst must determine how important the time-varying elements of the flow are to the overall behavior of the system. For one, in a time-varying approach, the governing fluid dynamics equations must be discretized in space and time. Not only does this complicate the set of algebraic equations the numerical solver must manipulate, but sub-iterations become necessary to compute a flow field solution for each instant of time. In other words, the solver must achieve a converged solution for each increment of time that the analyst has chosen to model. This can increase the total rate of convergence by several orders of magnitude and reduce the computational efficiency of the model to the point where the problem is no longer tractable. Also, since convergence of each sub-iteration must be attained prior to proceeding on to the next time step, the likelihood of solution oscillations or divergence is increased.

The major drawback in modeling a problem as steady-state is that the possibility exists that important aspects of the flow will be overlooked. For example, time-varying and periodic behaviors such as vortex mixing and vortex streets, and transient behaviors such as flow acceleration and deceleration will not be captured when using a steady-state approach. Again, intuition on the part of the fluid dynamicist is necessary to determine whether the omission of such aspects of the flow will have a large impact on the overall accuracy of the solution generated by the flow solver.

Chapter 5 – Numerical Simulation

The numerical simulation portion of this study was conducted in three distinct stages. First, computational models were created and simulations were run on laminar axisymmetric spheres, the results of which were compared to historical data to validate the computational models. Next, axisymmetric models were created representing each additional turret configuration that Snyder tested: the turret combined with a small aft-mounted fairing and the turret combined with a large aft-mounted fairing. A fourth configuration was designed and tested as well: an optimized aft-mounted fairing. Finally, for stage three, the flow fields computed about the four turret/fairing models in the first two stages were recomputed with the Spalart-Allmaras turbulence model activated.

5.1 Axisymmetric Laminar Spheres

5.1.1 Model Geometries and Boundary Conditions

To maintain consistency with Snyder's research and the dimensions of his turret model and to ease the addition of aft-mounted fairings in later stages of the project, 0.23 m diameter spheres were modeled. In fact, Snyder's clean turret was numerically modeled as an axisymmetric sphere. Computer platform limitations necessitated the use of axisymmetric models instead of full three-dimensional models. Given the grid densities required to adequately predict the flow field throughout the domains defined above, the use of fully-3D models was simply not possible – the problems would no longer be solvable in reasonable amounts of time. The axisymmetric grids used in this study were comprised of 10,000 to 30,000 cells. Assuming a similar node density in

three-dimensional space, a minimum of one million cells would be needed for 3D grids of equal resolution. Also assuming that an increase in CPU time is proportional to an increase in cell count, simulations that took two to four hours in the axisymmetric cases could take 200 to 400 hours using 3D models. This estimated increase in solution time is quite conservative – it does not consider computer platform memory limitations, additional terms required in the governing 3D fluid dynamics equations, or the additional faces added to each cell when moving from 2D to 3D. Though out-of-plane flow and complex 3D interactions (like vortex mixing) would not be modeled using axisymmetric simulations, enough similarities remained between the 3D experimental models and the axisymmetric numerical models to draw parallels between the Snyder's work and the computer simulations used in this study. This necessary simplification would still allow the numerical solutions to capture the majority of the physics taking place in these complex flow fields.

Although all of the sphere models were of the same dimensions, multiple models were built with different grids in order to analyze the effects on the solution of using different grid densities. GAMBIT's geometry sub-program was used to create the geometric models. First, it was necessary to determine the size of the numerical domain that would be used for the models. Based on intuition and the author's previous work in two-dimensional CFD modeling, the domain was extended horizontally fore and aft of the sphere and vertically upward ten times the sphere diameter (Figure 5.1). This ensured that the numerical results would be accurate, even when fairings were added to the domain aft of the sphere later, and that the problem would be solvable in a reasonable

amount of time. Since the geometry of an axisymmetric sphere is, in effect, a semicircle rotated about an axis parallel to the freestream velocity, the bottom boundary of the domain was modeled as an axis boundary (Figure 5.1). The axis boundary type must be used as the centerline of an axisymmetric geometry (Fluent Inc., 1998: 6-95). To determine the physical values for a particular variable at a point on the axis, FLUENT uses the cell value in the adjacent cell. Additionally, the left boundary of the domain was modeled as a velocity inlet, the top boundary was modeled as a wall, the right boundary was modeled as an outflow boundary, and the surface of the sphere itself was modeled as a wall. The velocity inlet boundary condition is intended for use with incompressible flows where the magnitude and direction of the inlet velocity is known. This boundary condition allows the stagnation, or total, properties of the flow to rise to whatever value is necessary to generate the prescribed velocity distribution. Since the conditions in a low-speed wind tunnel were being modeled, and the inlet velocity in Snyder's work was specified as 55 m/s ($M = 0.16$), this incompressible boundary condition was a good choice for this study. Specifying the boundary layer in this manner was not entirely consistent with Snyder's work, however, since his models were mounted on a flat surface upon which a boundary layer would form. The formation of this boundary layer would prevent the freestream velocity in Snyder's wind tunnel from being uniformly 55 m/s. The outflow boundary condition is used to model flow exits where the details of the flow velocity and pressure are not known prior to the solution of the problem. The user need define no conditions at the exit; FLUENT extrapolates the required information from the interior of the domain. As long as the flow at the exit is expected to be well-developed and incompressible (at it was in this study, given the geometry of the domain and the

freestream velocity), application of the outflow boundary condition to the exit boundary is a reasonable choice. Finally, the wall boundary condition is used to separate fluid and solid regions. In viscous flows (such as in this study), the no-slip, or zero tangential velocity boundary condition, is enforced when the wall boundary condition is imposed; the shear stress and associated friction drag is computed based on the flow details in the local flow field.

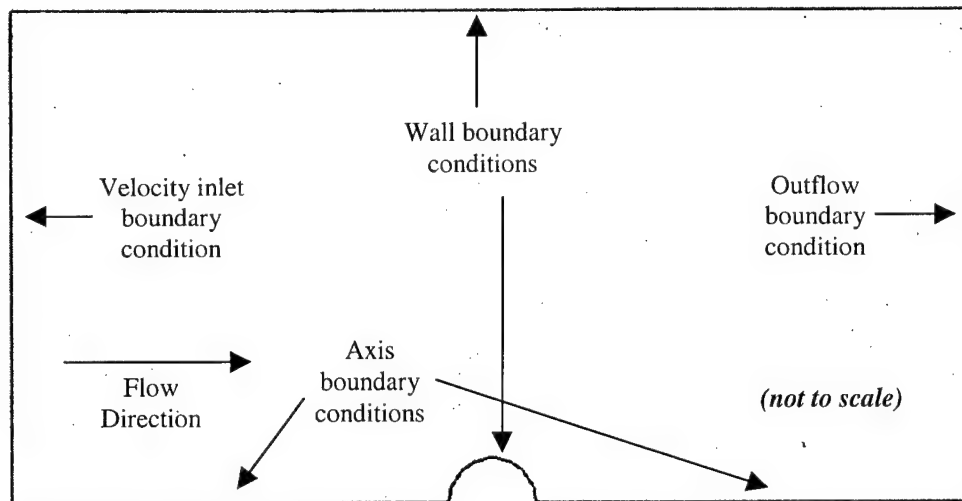


Figure 5.1. Axisymmetric sphere model geometry, domain, and boundary conditions, 5.06 m wide x 2.53 m high

5.1.2 Grid Construction

In this first stage of the project, two combinations of boundary node spacing were used to create two different grids based on the sphere's geometry described above. For the purposes of grid construction, the computational domain for each model was divided into two regions: the boundary layer region and the freestream region. Dividing the domain in this fashion is a common practice in problems where the effects of the viscous boundary layer that forms on the body are expected to significantly affect the flow field and where enhanced grid resolution in the vicinity of the boundary layer is important.

To define a boundary layer grid in GAMBIT, the following information must be specified:

- The face to which the boundary layer is attached
- The face that defines the direction of the boundary layer
- The height of the first row of boundary layer elements
- The growth factor (which specifies the height of each successive row of elements)
- The total number of rows (which defines the height of the boundary layer)

Two different sets of boundary layer grid parameters were used in this phase of the study, each of which corresponded to a freestream region grid (described later). The boundary layers were attached to the spheres and the direction of the boundary layer grids was defined such that the grids extended into the interior of the domains. Since the computed boundary layer thicknesses should not change because of grid resolution (assuming grid independence of the solution), the total height of the boundary layer grids was the same for both distributions. Based on prior experience with numerical simulations involving boundary layers and the expected growth of the boundary layer meridionally along the sphere, both boundary layer meshes were approximately 3 cm in height. Increasing the number of rows in the boundary layer meshes only served to vary cell density, and did not change the total height of the mesh. Finally, the growth factors were chosen to increase the resolution of the meshes at the base of the boundary layers (where flow parameter gradients are largest) while still maintaining high grid resolution, low cell skewness at the top of the boundary layers, and a total boundary layer mesh thickness of

approximately 3 cm. Low skewness was important to ensure similar cell proportions between outer boundary layer cells and neighboring freestream region cells. The boundary layer grid parameters for the axisymmetric sphere models are shown in Table 5.1, and Figures 5.2 through 5.3 depict the boundary layer grids for each node spacing combination. If the growth factor is not listed in the table it was equal to unity.

Table 5.1. Boundary layer parameters of axisymmetric sphere grids

	Meridional node count on sphere surface	First row thickness in boundary layer	Boundary layer growth factor	Number of rows in boundary layer
Mesh 1	100	0.0001	1.24	20
Mesh 2	150	6.66×10^{-5}	1.153	30

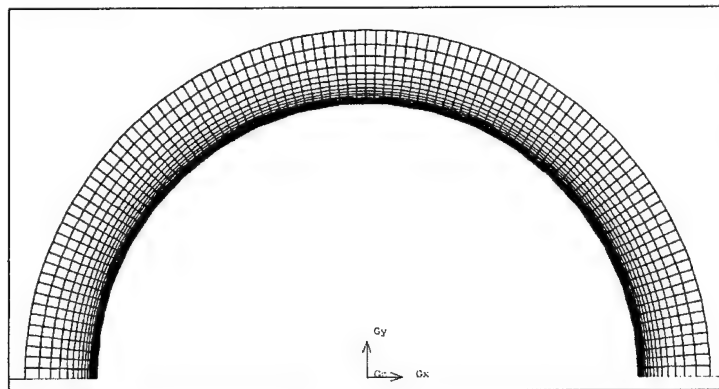


Figure 5.2. Mesh 1 boundary layer grid

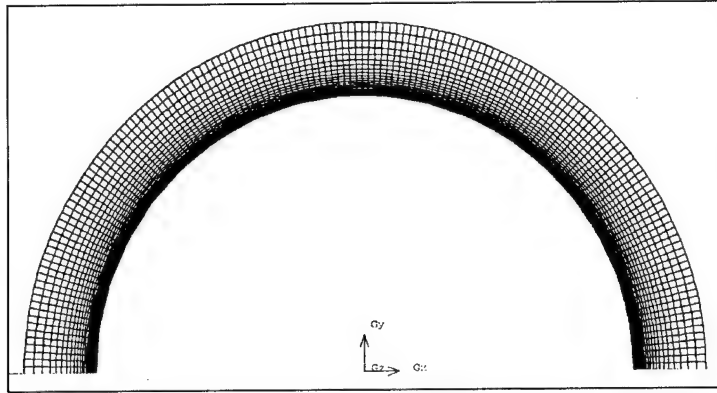


Figure 5.3. Mesh 2 boundary layer grid

Meshing of the freestream regions took place in two steps. First, the edges of the regions were meshed, and then, using the edge meshes, the interiors of the regions (or faces) were meshed. To perform an edge mesh operation in GAMBIT I, the following parameters need to be specified:

- Edge to be meshed
- Grading scheme
- Node spacing or number of intervals

Since boundary layer meshing had already been performed, only the axis boundary, inlet, outlet, and top edges had to be meshed. Comparatively course meshes were specified on the exterior (inlet, outlet, and top) boundaries due to the expected lack of large flow property fluctuations (and thus low grid densities) in those regions. Two different overall edge node distributions were used (called Mesh 1 and Mesh 2). Grading, which determines the ratio of successive node separation distances along a given edge, was only applied on the symmetry surfaces. For better control of edge node spacing, the bottom boundary was constructed in multiple sections as shown in Figure 5.4. Grading was necessary to ensure a smooth transition between the relatively small cell sizes near the

boundary layer grids and the relatively large cell sizes on the outer edges of the domains. Table 5.2 shows the node spacing on the edges of the domains for each edge node distribution.

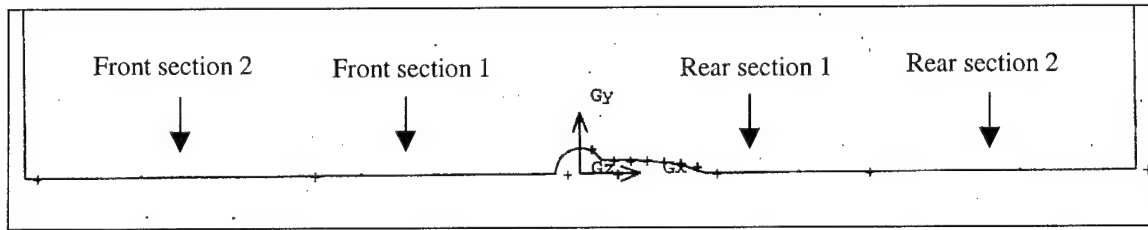


Figure 5.4. Axisymmetric bottom boundary sections

Table 5.2. Axisymmetric sphere boundary node spacing distributions

	Node count on front section 1	Growth factor on front section 1	Node count on front section 2	Node count on rear section 1	Growth factor on rear section 1	Node count on rear section 2	Node count on inlet/exit boundary	Node count on top boundary
Mesh 1	50	0.9	12	50	1.111	12	20	40
Mesh 2	75	0.94	15	75	1.064	15	30	60

Once the edges were meshed, the interior of the domains had to be meshed. In order to use GAMBIT I's automatic face mesh generation scheme, the following data was required:

- Meshing scheme
- Mesh node spacing

The meshing scheme that was chosen was Pave meshing scheme. The Pave scheme creates an unstructured grid of mesh elements, which is particularly desirable for its

applicability to a wide range of face geometries, its ability to deal with irregularly shaped interiors, and its ease of use. In the interest of consistency and efficiency, unstructured meshes were used for all face grids in this study. As mentioned earlier, the Mesh 1 boundary layer grid was only matched with the Mesh 1 freestream region mesh and the Mesh 2 boundary layer grid was only matched with the Mesh 2 freestream region mesh. Finally, since the edges previously meshed defined the edges of the faces to be meshed by the Pave scheme, there was no need to further specify the mesh node spacings. There was no restriction on mesh node spacing imposed by the Pave scheme since only triangular face elements were used; preliminary work with quadrilateral element-based grids uncovered difficulties in successfully generating complete quad meshes with the Pave scheme. Figures 5.5 and 5.6 show both full axisymmetric sphere grids that were generated by GAMBIT.

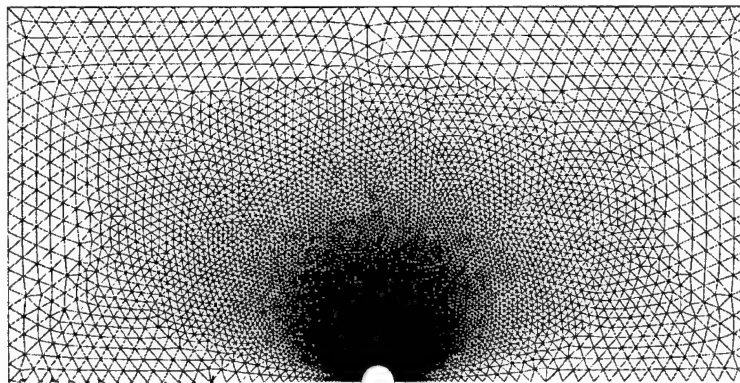


Figure 5.5. Mesh 1, axisymmetric sphere

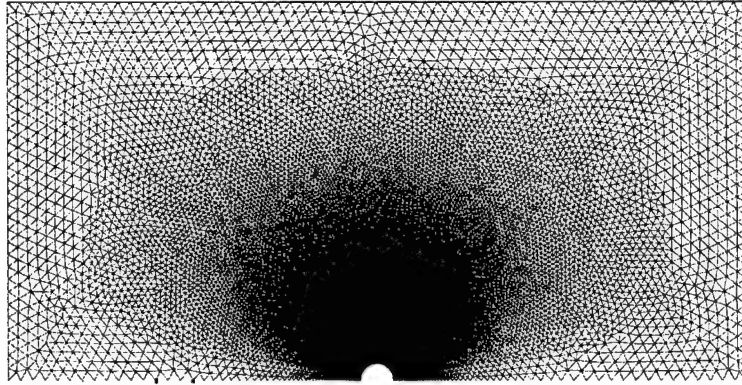


Figure 5.6. Mesh 2, axisymmetric sphere

5.1.3 Solver Initialization and Flow Solution

After the grids were constructed, the next step was to import them into FLUENT 5, the numerical solver. Since each grid was exported from GAMBIT I in FLUENT 5's native format, the import process was straightforward. After the grids were imported, the solver was initialized. This procedure involved several steps; among them:

- Selecting the solver formulation
- Defining physical models
- Specifying fluid properties
- Specifying boundary conditions
- Adjusting solution controls
- Initializing the flow field
- Iterating

For all of the grids generated in this study, the segregated solver formulation (FLUENT 5's default) was used. This approach solves the continuity, momentum, and energy equations sequentially as opposed to simultaneously. Because the segregated solver is

traditionally used for incompressible and mildly compressible flows, given the flow conditions being investigated, this study was well-tailored for its use. Also, the solution controls (under-relaxation parameters, etc) were left at the default settings for all cases. Next, the flows around all of the geometries modeled in this study were approximated as steady-state. Although this choice precluded the ability to capture vortex shedding and other time-dependent effects, the majority of pertinent flow features and their associated drag effects (like separation point, pressure drag, and skin friction drag) could still be accurately modeled. One reason for choosing steady-state simulations was because of the reduced computational load they placed on the computer – given the total number of simulations needed, run time was a major limiting factor. The other, more compelling reason for choosing a steady-state modeling approach was that the properties of interest in this study are all steady state values. Although, in reality, separation point, skin friction, pressure, and drag all vary with respect to time on a microscopic scale, their net values and net effects can usually be considered steady properties and can accurately be modeled as such.

For all geometries modeled in this thesis, definition of the physical models simply involved specifying whether a laminar or turbulent simulation was desired and whether the energy equations would be used in the solution computation. For the axisymmetric sphere models in stage one, laminar solutions were sought to compare with data in the open literature, so laminar models were specified. Since predicting the effects of heat transfer was not required and since viscous dissipation was not modeled for any of this project's simulations, these options were not selected.

Specifying the fluid properties and the boundary conditions was very straightforward. For every computational model in the study, the default fluid properties for air (air at standard conditions) were used. Also, the boundary condition types were all specified during the grid generation step, so the only addition needed was to specify the inlet velocity and direction; this was 55 m/s normal to the inlet boundary for all numerical models. These conditions were chosen to closely model the operating conditions in Snyder's work (Snyder, 1998: 28).

For all flow cases, the flow field was initialized from the inlet boundary condition. This process was necessary to provide a starting point for the evolution of the iterative solution process. In every case, after the flow was successfully initialized, the solution was iterated until one of the following three conditions was attained: convergence, divergence, or non-decaying oscillation of the residuals. Convergence was declared if the x-velocity, y-velocity, and continuity residuals all dropped below 0.001.

5.2 Axisymmetric Laminar Turret Models

5.2.1 Model Geometries and Boundary Conditions

For this stage of the project, the physical dimensions of the aft-mounted fairings used in Snyder's work were measured and approximate computational models were created. For reasons that were discussed in Section 5.1.1, the three-dimensional physical models were numerically modeled as axisymmetric bodies of rotation. A procedure to convert the physical 3D geometries to axisymmetric numerical models was devised.

First, a line was drawn on both sides of each fairing model to represent the location of the centerline of the spherical part of the turret (Figure 5.7). Next, the width of each fairing at the spherical centerline was measured at several axial stations aft of the contact point between the turret and each fairing (Figure 5.8). The stations were spaced three inches apart. Finally, the width measurements were divided in half to provide the radial coordinates of the axisymmetric numerical fairing model. Since both the axial coordinates (positions of axial stations) and the radial coordinates (half of the width measurements) of the new numerical fairing models were then known, this data was entered into GAMBIT I to define the shapes of the axisymmetric turret/fairing models. The turret/fairing combinations were modeled as spheres up to the contact point between the turret and the fairing, and the clean turret was simply modeled as an axisymmetric sphere with a diameter of 0.23 m. GAMBIT's curve-fit command was used to create smooth surfaces from the coordinate data entered. The coordinates of the small and large fairing models are listed in Table 5.3 and Table 5.4, respectively. Pictures of the small fairing/turret model and large fairing/turret model are shown in Figure 5.9 and Figure 5.10, respectively.

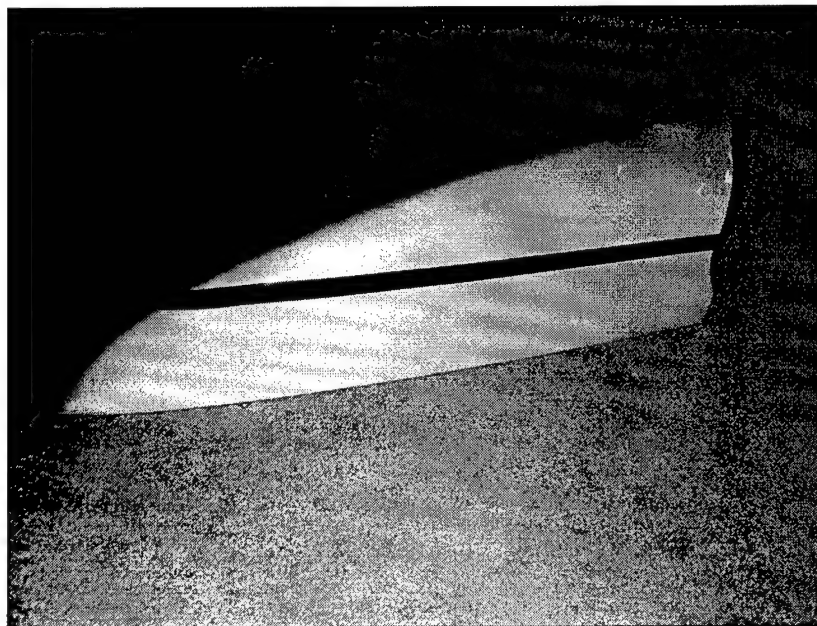


Figure 5.7. Location of spherical centerline of turret extended onto large fairing model

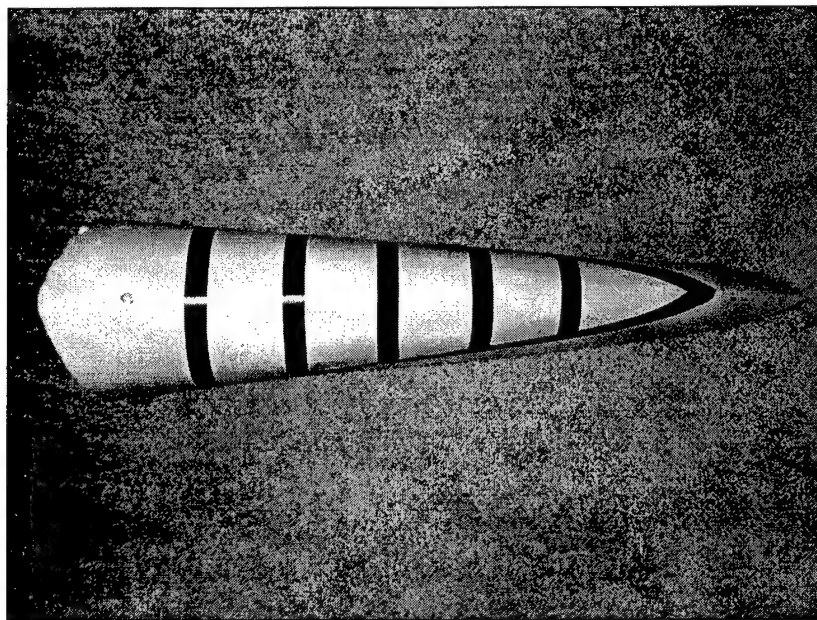


Figure 5.8. Location of width measurements taken on large fairing model

Table 5.3. Axial and radial coordinates of small axisymmetric fairing numerical model

Axial coordinate (cm)	9.9	17.5	25.1	32.7	40.3	48.0	57.2
Radial coordinate (cm)	5.9	5.9	5.9	5.5	4.7	3.1	0

Table 5.4. Axial and radial coordinates of large axisymmetric fairing numerical model

Axial coordinate (cm)	8.7	16.4	24.0	31.6	39.2	46.8	57.3
Radial coordinate (cm)	7.5	6.7	5.9	5.1	4.3	3.3	0

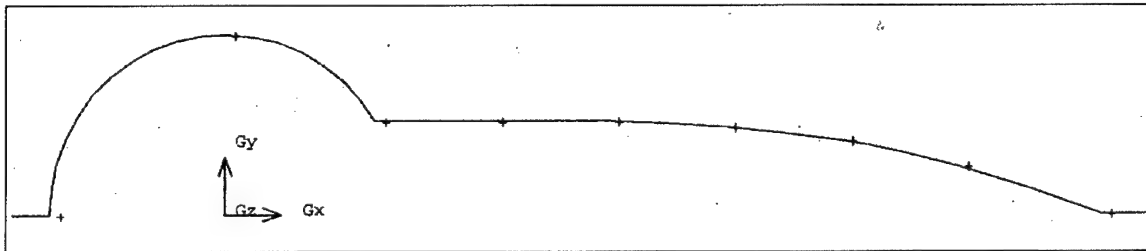


Figure 5.9. Axisymmetric model of small fairing/turret combination

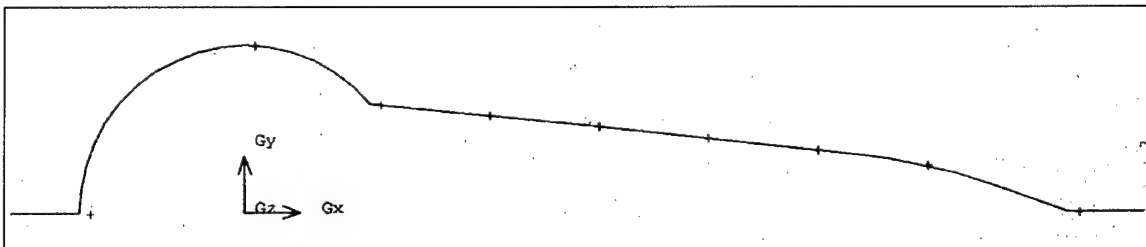


Figure 5.10. Axisymmetric model of large fairing/turret combination

Since an optimal configuration for drag reduction would be to create a fairing flush with the top of the turret that would hopefully eliminate any separation regions and their associated wake pressure drag, such a design was used to create the optimized turret

model. Although no optimization studies were carried out, this new fairing was called “optimized” because of the lack of geometric discontinuities it produced when coupled with the sphere. The inherent smoothness of this geometry is conducive to the elimination of separation regions and the reduction of pressure drag. Of course, the real-world trade-off for such a large fairing would be a 60-degree reduction in look angle available to the laser system, though this might be alleviated with further optimization.

The axial coordinates of the optimized fairing were carried over from the small fairing; however, a weighted average between the turret’s radius and the small fairing’s radial coordinates was taken to generate the radial coordinates for the optimized fairing. The formula used for the optimized fairing’s coordinates aft of the turret’s apex was as follows:

$$r_{optimized} = r_s + (r_t - r_s) \left(1 - \frac{i}{n} \right)$$

where

- $r_{optimized}$ = radial coordinate of optimized fairing
- r_s = radial coordinate of small fairing model
- r_t = radius of spherical turret model
- i = i th coordinate of small fairing aft of turret apex
- n = total number of coordinates in small fairing model

For example, since seven coordinates were used to define the geometry of the small fairing model, the second radial coordinate (in centimeters) aft of the turret’s apex of the optimized fairing model would be computed as

$$r_{optimized} = 6.7 + (11.5 - 6.7) \left(1 - \frac{2}{7} \right) = 9.1$$

The coordinates of the optimized fairing model are shown in Table 5.5 and a picture of the optimized fairing/turret model is shown in Figure 5.11.

Table 5.5. Axial and radial coordinates of optimized fairing numerical model

Axial coordinate (cm)	8.7	16.4	24.0	31.6	39.2	46.8	57.3
Radial coordinate (cm)	10.9	10.1	9.1	7.9	6.3	4.4	0

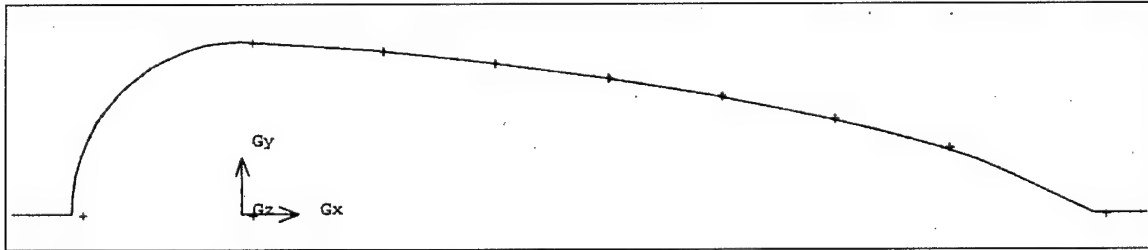


Figure 5.11. Axisymmetric model of optimized fairing/turret combination

Boundary conditions used for the axisymmetric laminar turret/fairing models were identical to those used for the axisymmetric sphere models.

5.2.2 Grid Construction

The size of the domain used for the axisymmetric turret/fairing models was identical to that used for the axisymmetric sphere models. In addition, the edge boundary conditions were also carried over from the stage one grids.

Three turret/fairing models now existed that required grid generation: the small turret/fairing model, the large turret/fairing model, and the optimized turret fairing model.

Two triangular element-based grids of different mesh densities were created for each turret/fairing model. The overall procedure for generating grids on these models was the same as that outlined in Section 5.1.2; the main difference was that the rear section node spacing could not be directly carried over from the earlier grids due to the added length of the fairings. Instead, it (and the spacing of the bottom sections) was slightly modified in order to maintain a smooth, even node distribution between the boundary layer and the exit boundary. Also, although the boundary layer grids were longer in this stage due to the added length of the fairing, the meridional node spacings, row counts, and growth factors were identical to those used in the corresponding sphere grids. Table 5.6 lists the boundary layer parameters and edge node distributions for the axisymmetric turret/fairing grids, Figures 5.12 through 5.17 show the new boundary layer grids, and Figures 5.18 through 5.23 depict the entire axisymmetric grids for each turret/fairing combination. Again, if the growth factor is not listed in the table, it was equal to unity.

Table 5.6. Boundary node distributions on axisymmetric turret/fairing grids

	Meridional node spacing on body surface	First row thickness in boundary layer	Boundary layer growth factor	Number of rows in boundary layer	Node count on front section 1	Growth factor on front section 1	Node count on front section 2	Node count on rear section 1	Growth factor on rear section 1	Node count on rear section 2	Node count on inlet/exit boundary	Node count on top boundary
Mesh 1 small fairing	.003613	.0001	1.24	20	50	0.9	12	50	1.15	12	20	40
Mesh 1 large fairing	.003613	.0001	1.24	20	50	0.9	12	50	1.15	12	20	40
Mesh 1 optimized fairing	.003613	.0001	1.24	20	50	0.9	12	50	1.15	12	20	40
Mesh 2 small fairing	.002409	6.66×10^{-5}	1.153	30	75	0.94	15	75	1.1	18	30	60
Mesh 2 large fairing	.002409	6.66×10^{-5}	1.153	30	75	0.94	15	75	1.1	18	30	60
Mesh 2 optimized fairing	.002409	6.66×10^{-5}	1.153	30	75	0.94	15	75	1.1	18	30	60

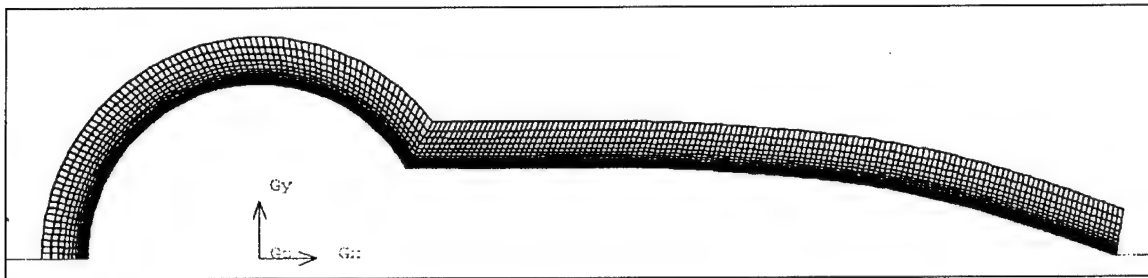


Figure 5.12. Mesh 1, small fairing/turret combination boundary layer grid

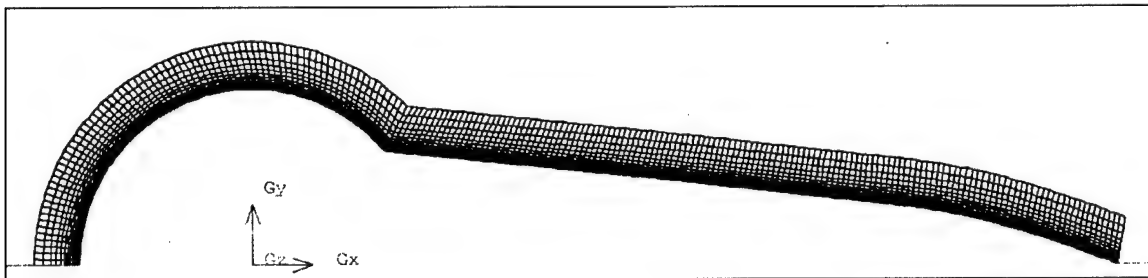


Figure 5.13. Mesh 1, large fairing/turret combination boundary layer grid

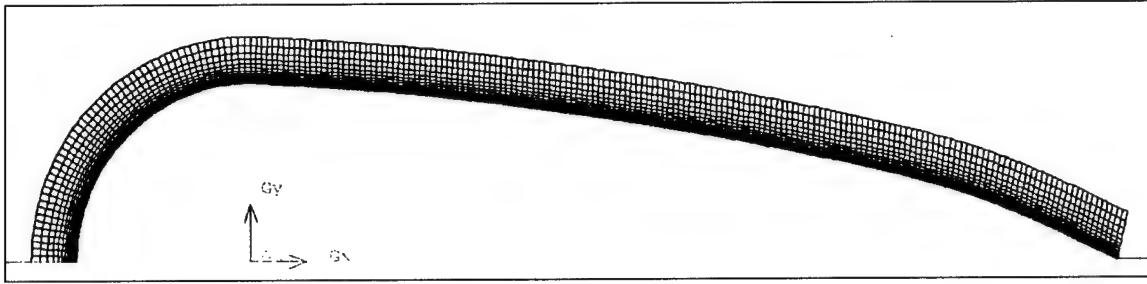


Figure 5.14. Mesh 1, optimized fairing/turret combination boundary layer grid

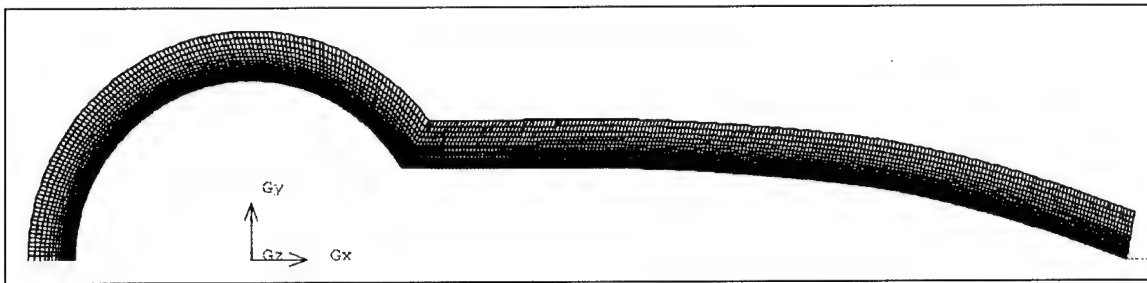


Figure 5.15. Mesh 2, small fairing/turret combination boundary layer grid

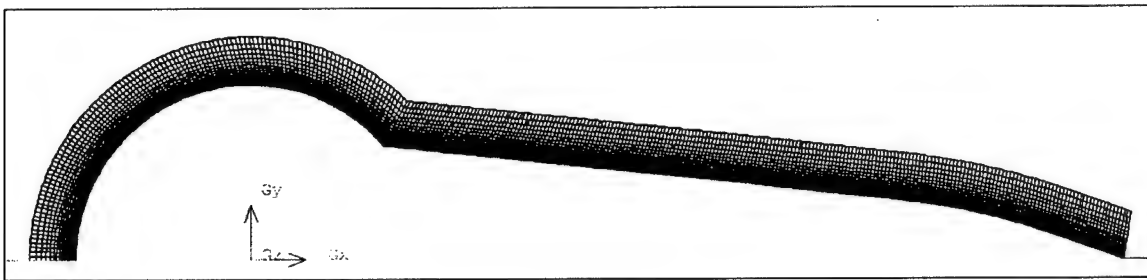


Figure 5.16. Mesh 2, large fairing/turret combination boundary layer grid

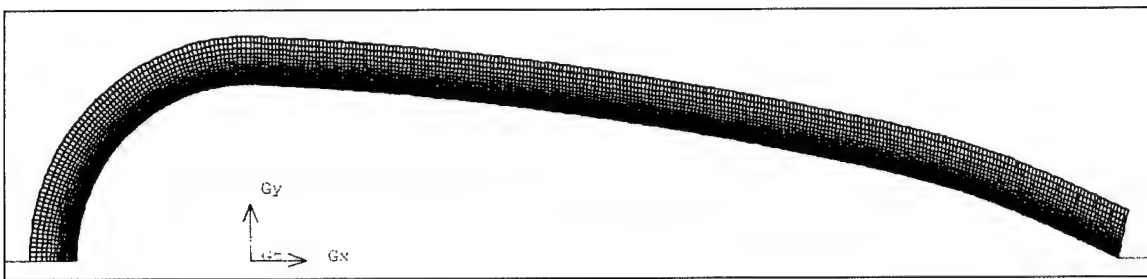


Figure 5.17. Mesh 2, optimized fairing/turret combination boundary layer grid

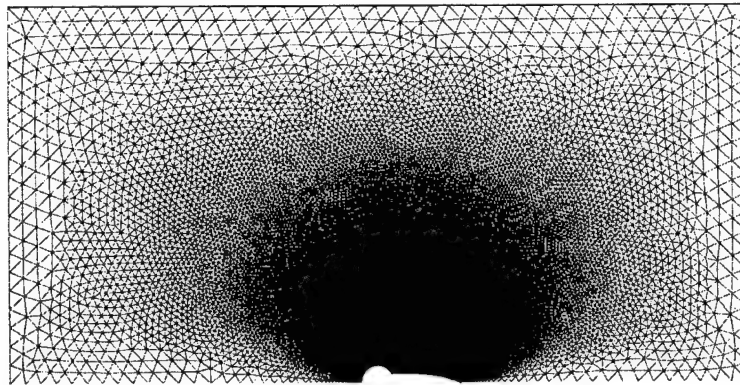


Figure 5.18. Mesh 1, small fairing/turret combination

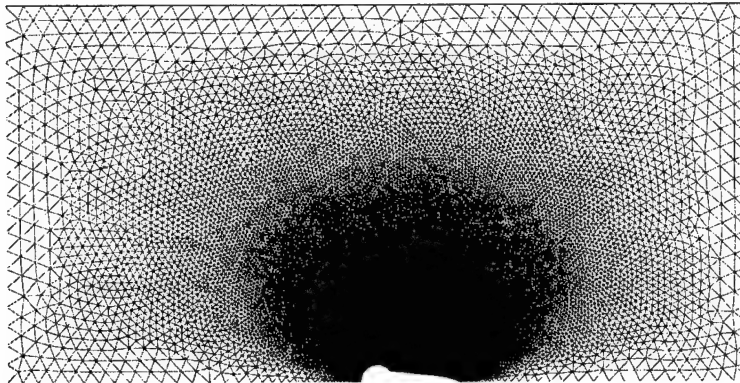


Figure 5.19. Mesh 1, large fairing/turret combination

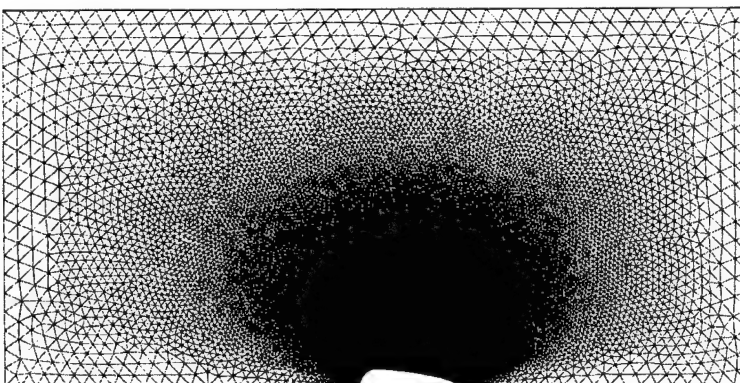


Figure 5.20. Mesh 1, optimized fairing/turret combination

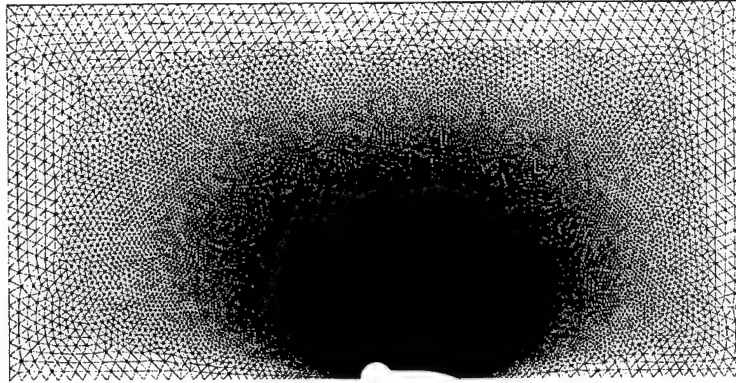


Figure 5.21. Mesh 2, small fairing/turret combination

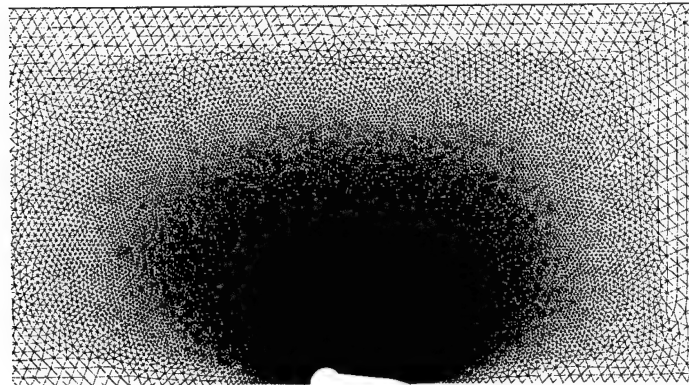


Figure 5.22. Mesh 2, large fairing/turret combination

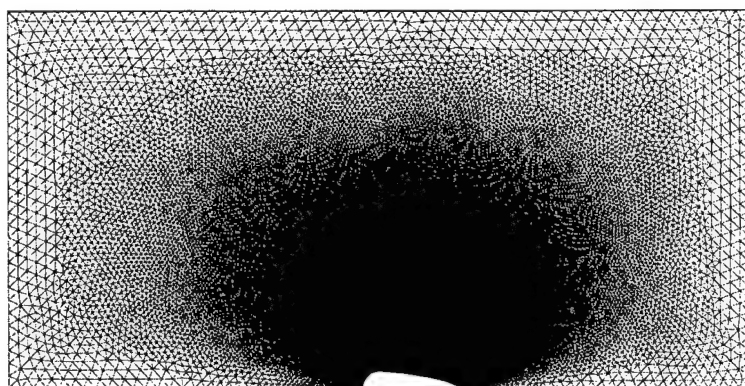


Figure 5.23. Mesh 2, optimized fairing/turret combination

5.2.3 Solver Initialization and Flow Solution

The solver initialization and flow solution procedure in this stage was identical to that used in stage one.

5.3 Axisymmetric Turbulent Turret Models

The only difference between the first and second stage (axisymmetric laminar) models and third stage (axisymmetric turbulent) models used in this work was the implementation of the Spalart-Allamas turbulent model in the third stage instead of the laminar model. All of the grids used in the third stage were identical to the ones generated in the first two stages. Aside from the implementation of the turbulence model, the solver initialization and flow solution procedures were identical as well. FLUENT's default turbulence model constants were used for each run, and the default turbulent viscosity of 0.1 was specified.

Chapter 6 – Results and Discussion

One major benefit of CFD analysis is its ability to compute the values of every flow parameter at every grid point in the domain studied, giving a very descriptive picture of the entire flow field. Because of this, each converged solution of the computational models described in Chapter 5 provided a wealth of information about its respective flow field. However, for the purposes of comparison with historical data, Snyder's data, and for drag prediction, four main values were focused on in this thesis: pressure coefficient, skin friction coefficient, drag coefficient, and boundary layer separation point. All of these values were computed on the surface of the body being studied. Velocity vector plots were also used when necessary to visualize the flow field.

6.1 Definitions

Because FLUENT 5 operates in terms of gauge pressures, the pressure coefficient was defined as

$$C_p = \frac{p_{gauge}}{\frac{1}{2} \rho_{ref} V_{ref}^2}$$

where

$$\begin{aligned} p_{gauge} &= \text{gauge pressure} \\ \rho_{ref} &= \text{reference density} \\ V_{ref} &= \text{reference velocity} \end{aligned}$$

This definition is similar to the usual definition of pressure coefficient

$$C_p = \frac{p - p_{ref}}{\frac{1}{2} \rho_{ref} V_{ref}^2}$$

since

$$p_{gauge} = p - p_{ref}$$

Reference conditions in FLUENT 5 are entered by the user. For this study, reference conditions were taken as those values for air at standard temperature and pressure; in other words

$$p_{ref} = 1.01325 \times 10^5 \text{ N/m}^2$$

$$\rho_{ref} = 1.225 \text{ kg/m}^3$$

$$\mu_{ref} = 1.7894 \times 10^{-5} \text{ kg/m} \cdot \text{s}$$

The location of the reference pressure was always given as on the lower edge of the inlet boundary. The reference velocity was chosen as 55 m/s because that was the experimental inlet boundary condition.

The drag coefficient was defined as

$$C_D = \frac{D}{\frac{1}{2} \rho_{ref} V_{ref}^2 S}$$

where

D = drag force

S = turret or turret/fairing combination frontal area

Since for this study, the projected frontal area of the simulated turret or turret/fairing combination was always a circle, then

$$S = \pi r_{turret}^2 = \pi (.115 \text{ m})^2 = 0.04155 \text{ m}^2$$

As explained earlier, the drag force D consisted of two parts: the pressure drag and the skin friction drag. Pressure drag is simply the component of the pressure force acting in the axial direction. Skin friction drag is a function of the fluid viscosity and the velocity profile at the surface of the body. FLUENT 5 directly computed both pressure drag and skin friction drag by numerically integrating the incremental value of each at every node point along the body surface.

The skin friction coefficient was defined as

$$C_f = \frac{\tau_w}{\rho_{ref} V_{ref}^2} \sqrt{\text{Re}_D}$$

where

τ_{wall} = wall shear stress

Re_D = Reynolds number based on turret diameter

FLUENT 5 directly calculated the wall shear stress, and the Reynolds number for this study was computed as

$$\text{Re}_D = \frac{\rho_{ref} V_{ref} D_{turret}}{\mu_{ref}} = 8.66 \times 10^5$$

The boundary layer separation point occurs when skin friction on a body surface goes to zero. Thus, it was simple to determine the boundary layer separation point for each computational model by analyzing plots of C_f versus meridional angle (for the

sphere cases) or axial position (for the turret/fairing combinations). Since FLUENT 5 only generated plots of the absolute value of C_f , it was impossible to directly plot zero-crossings since no negative values of C_f were shown, but the zero-crossing points could still be fairly accurately interpolated from the graphs.

Percent difference was calculated in two ways. First, for separation angle, percent difference was found by using the formula

$$\% \text{ difference } \phi = \frac{|\phi_{calc} - \phi_{ref}|}{\phi_{ref}} \times 100$$

where

ϕ_{calc} = separation angle calculated by FLUENT 5

ϕ_{ref} = reference separation angle from experimental data

Drag coefficient percent difference was computed in a similar fashion, namely

$$\% \text{ difference } C_D = \frac{|C_{D_{calc}} - C_{D_{ref}}|}{C_{D_{ref}}} \times 100$$

where

$C_{D_{calc}}$ = drag coefficient calculated by FLUENT 5

$C_{D_{ref}}$ = reference drag coefficient from experimental data

The second way in which percent difference was computed applied to the minimum pressure and maximum skin friction coefficient difference calculations. This method was used in order to present an objective measure of the maximum difference between the computed data and the experimental data for the C_p and C_D data sets. For these data sets, percent difference was calculated relative to the data range. For example, percent difference in minimum computed pressure coefficient was found by using the formula

$$\% \text{ difference } C_{p_{\min}} = \frac{|C_{p_{\min,calc}} - C_{p_{\min,ref}}|}{|C_{p_{\max,ref}} - C_{p_{\min,ref}}|} \times 100$$

where

$C_{p_{\min,calc}}$ = minimum pressure coefficient calculated by FLUENT 5

$C_{p_{\min,ref}}$ = minimum reference pressure coefficient from experimental data

$C_{p_{\max,ref}}$ = maximum reference pressure coefficient from experimental data

Percent difference in maximum computed skin friction coefficient was calculated similarly, namely

$$\% \text{ difference } C_{f_{\max}} = \frac{|C_{f_{\max,calc}} - C_{f_{\max,ref}}|}{|C_{f_{\max,ref}} - C_{f_{\min,ref}}|} \times 100$$

where

$C_{f_{\max,calc}}$ = maximum skin friction coefficient calculated by FLUENT 5

$C_{f_{\min,ref}}$ = minimum reference skin friction coefficient from experimental data

$C_{f_{\max,ref}}$ = maximum reference skin friction coefficient from experimental data

6.2 Axisymmetric Laminar Turret Model Results

6.2.1 Comparison of Axisymmetric Laminar Sphere Results to Experimental Data

For the first portion of the axisymmetric laminar study, the results computed from the two clean turret (sphere) grids discussed in Section 5.1 were compared to historical data for sub-critical laminar flow ($Re=1.62 \times 10^5$) past a sphere. In Figure 6.1 and Table 6.1, the pressure coefficient plots and difference percentages in minimum computed pressure coefficient for each sphere grid are shown, respectively.

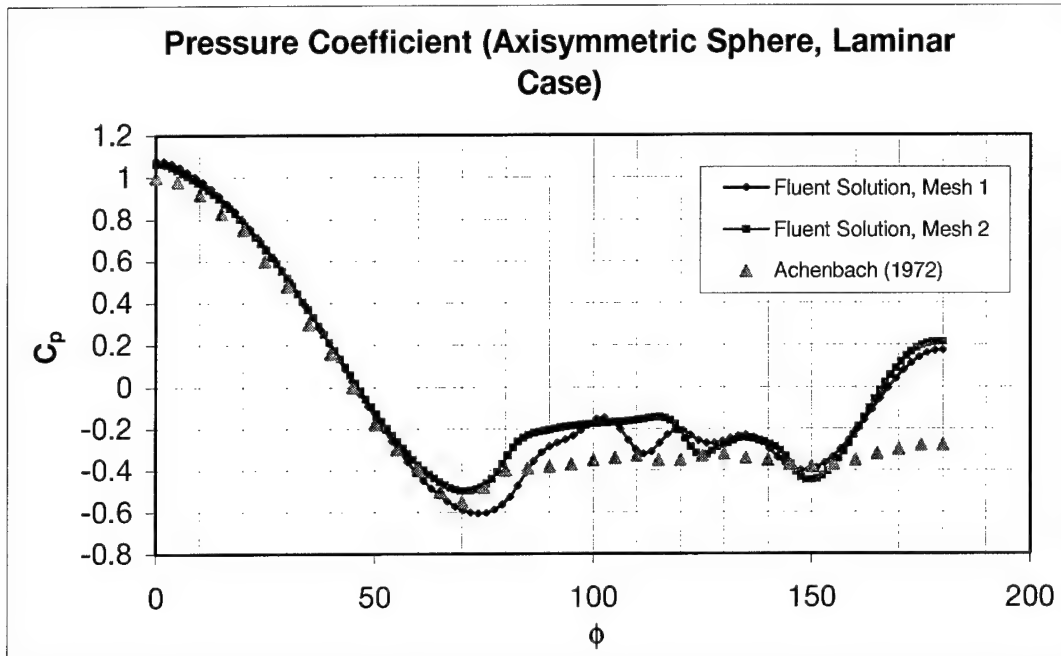


Figure 6.1. Pressure coefficient (axisymmetric sphere, laminar case) plots

Table 6.1. Percent difference in minimum computed pressure coefficient for axisymmetric laminar sphere cases versus Achenbach (1972)

	Mesh 1	Mesh 2
Percent difference, $C_{p, min}$	3.6 %	3.4 %

The computed pressure value curves followed the experimental curve very closely for the flow region forward of the separation point. Aft of the separation point, the differences in pressure coefficient were largely due to turbulent eddies present in the real flow that were not modeled in the computational laminar flow.

Figure 6.2 and Table 6.2 show the skin friction coefficient plots and difference percentages of maximum computed skin friction coefficient for each sphere grid.

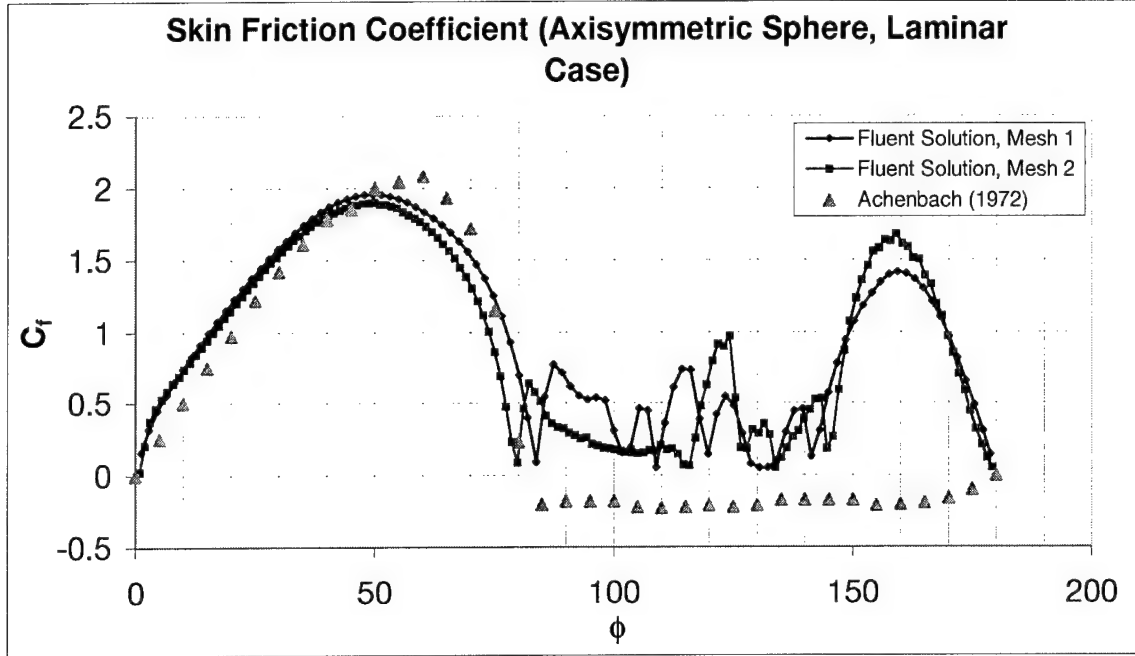


Figure 6.2. Skin friction coefficient (axisymmetric sphere, laminar case) plots

Table 6.2. Percent difference in maximum computed skin friction coefficient for axisymmetric laminar sphere cases versus Achenbach (1972)

	Mesh 1	Mesh 2
Percent difference, $C_{f, max}$	5.3 %	7.8 %

It was difficult to draw accurate conclusions about the accuracy of the skin friction coefficient values computed numerically aft of the separation point since FLUENT 5 only reported the absolute value of C_f . However, the direction of the skin friction force was taken into account when FLUENT 5 computed the drag due to skin friction. Nevertheless, the C_f curves predicted numerically by FLUENT 5 followed Achenbach's experimental data extremely closely up to the point of separation. Also, due to the fully laminar flow condition imposed on the FLUENT 5 solver for this particular portion of the

study, it was unlikely that the skin friction coefficients predicted by the numerical solver would match the experimental data very well in the separated region; since the separated region is a largely turbulent zone, the skin friction imposed by this zone was expected to be considerably higher than that imposed by a otherwise similar laminar zone. This fact was not expected to have a large influence of the accuracy of the predicted drag coefficient, though, since skin friction drag only accounts for one to five percent of the total drag on a laminar sphere (Achenbach, 1972: 574). The skin friction and pressure coefficient plots also showed that grid density did not have a significant effect on the accuracy of the numerical results with respect to each other. In other words, grid independence was achieved.

In Table 6.3 the separation points associated with the skin friction coefficient plots and the difference percentages of computed separation points are shown for both laminar sphere cases.

Table 6.3. Separation points in degrees and difference percentages for axisymmetric laminar sphere cases

	Achenbach (1972)	Mesh 1	Mesh 2
Separation point (degrees)	82	84	80
Percent difference	n/a	2.4 %	2.4 %

Again, the numerical separation point predictions were extremely accurate compared to Achenbach's data.

Table 6.4 shows the drag coefficients and difference percentages in computed drag coefficients for both laminar sphere cases.

Table 6.4. Drag coefficients and difference percentages for axisymmetric laminar sphere cases

	Achenbach (1972)	Mesh 1	Mesh 2
Drag coefficient, C_D	0.5	0.334	0.352
Percent difference	n/a	33.2 %	29.6 %

Differences in the drag coefficients between the numerical simulations and the Achenbach's experimental data were attributed to the greater pressure recovery predicted by the numerical models as shown in Figure 6.1. This higher pressure recovery corresponds to higher pressures on the aft surface of the sphere. These higher pressures on the back of the sphere effectively pushed the sphere forward, reducing the total drag.

It was not useful to make direct comparisons between Snyder's experimental data and the computed axisymmetric laminar data since the real flow underwent a transition from laminar to turbulent and the bulk of the drag-producing effects (such as flow separation and wake formation) took place in the turbulent region of the flow. Such a comparison was made in the turbulent study discussed in Section 6.3. As will be discussed later, Snyder's separation point data indicated that separation took place in a turbulent flow region. However, because the real turret will encounter a fully laminar flow condition at some point in its operating envelope, it was still useful to determine if the fairing geometries had a measurable effect on drag reduction in a fully laminar flow.

Specifically, the ability of the aft-mounted fairings to reduce or eliminate the separation region in a laminar flow field was investigated.

6.2.2 Effects of Aft-Mounted Fairings on Drag Reduction in Laminar Flow Field

Figure 6.3 shows the skin friction coefficient plots for all four Mesh 1 numerical models (clean turret, small fairing/turret combination, large fairing turret/fairing combination, and optimized fairing/turret combination). Likewise, Figure 6.4 shows the skin friction coefficient plots for all four Mesh 2 numerical models. Table 6.5 shows the associated separation points for all of the Mesh 1 and Mesh 2 geometries. The $x=0$ coordinate corresponds to the sphere center point for all geometries.

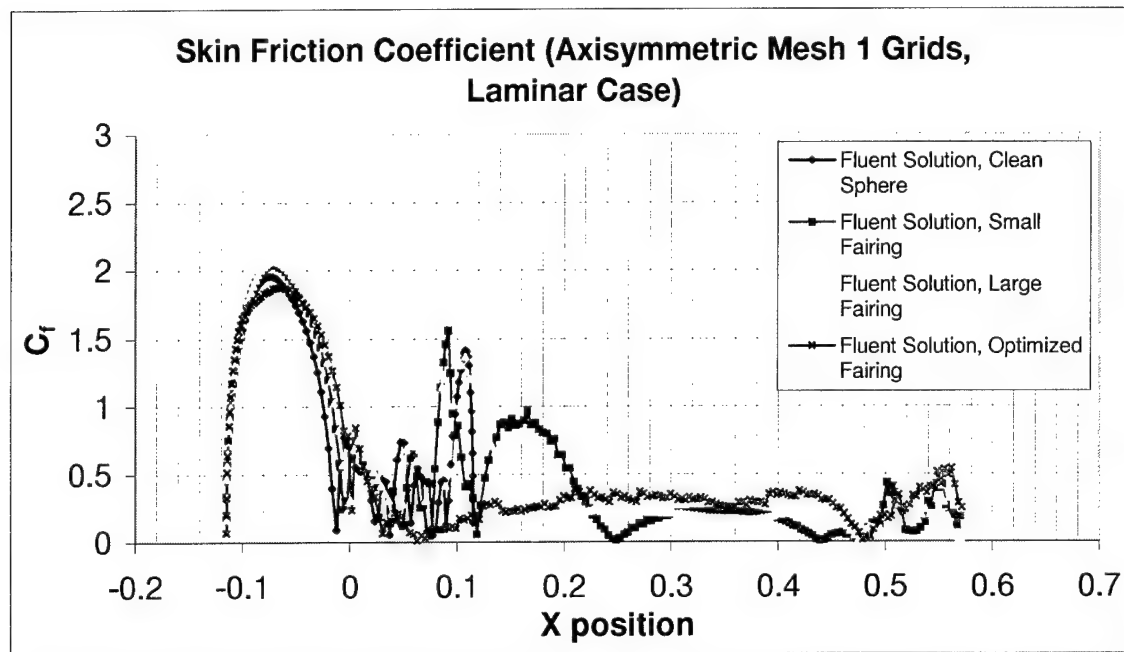


Figure 6.3. Skin friction coefficient (axisymmetric Mesh 1 grids, laminar case) plots

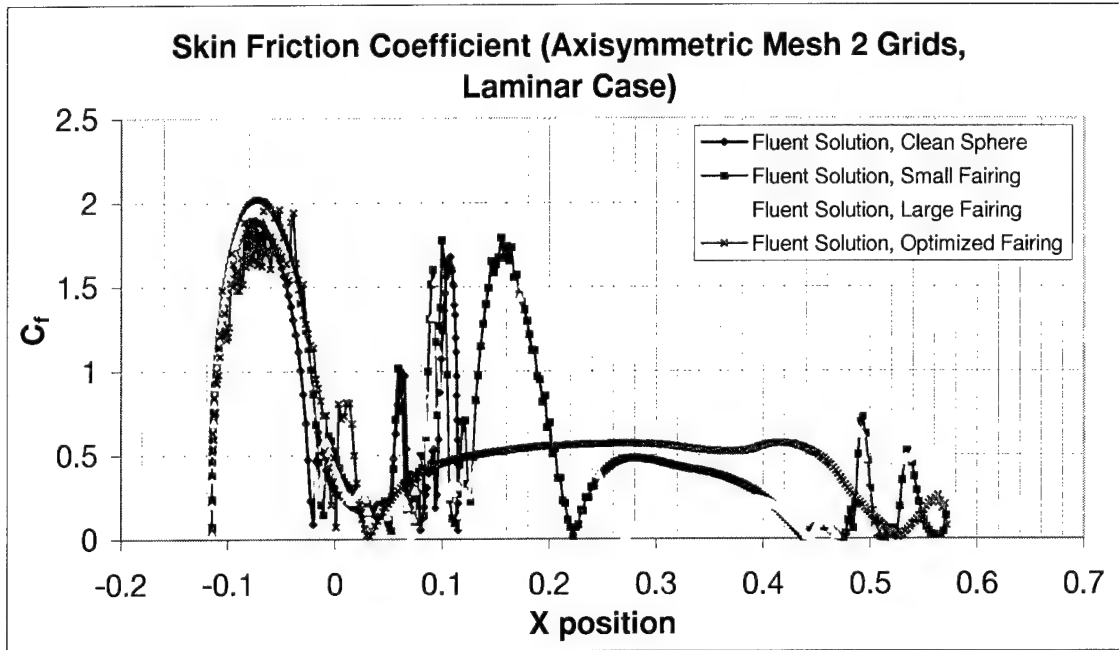


Figure 6.4. Skin friction coefficient (axisymmetric, Mesh 2 grids, laminar case) plots

Table 6.5. Separation points in degrees for all axisymmetric laminar grids

	Mesh 1	Mesh 2
Clean sphere separation point (degrees)	84	80
Small fairing separation point (degrees)	85	85
Large fairing separation point (degrees)	87.5	82
Optimized fairing separation point (degrees)	90	90

As can be seen from the C_f plots and Table 6.5, all of the axisymmetric models, regardless of fairing configuration, predict similar boundary layer separation locations. In addition, velocity vector plots (Figures 6.5-6.8) of the domains of the Mesh 2 models show a similar appearance (grid densities notwithstanding) among the separated regions of the small fairing, large fairing and clean turret models. Mesh 1 velocity vector plots

show a similar phenomenon, but Mesh 2 plots were included because of their higher resolution.

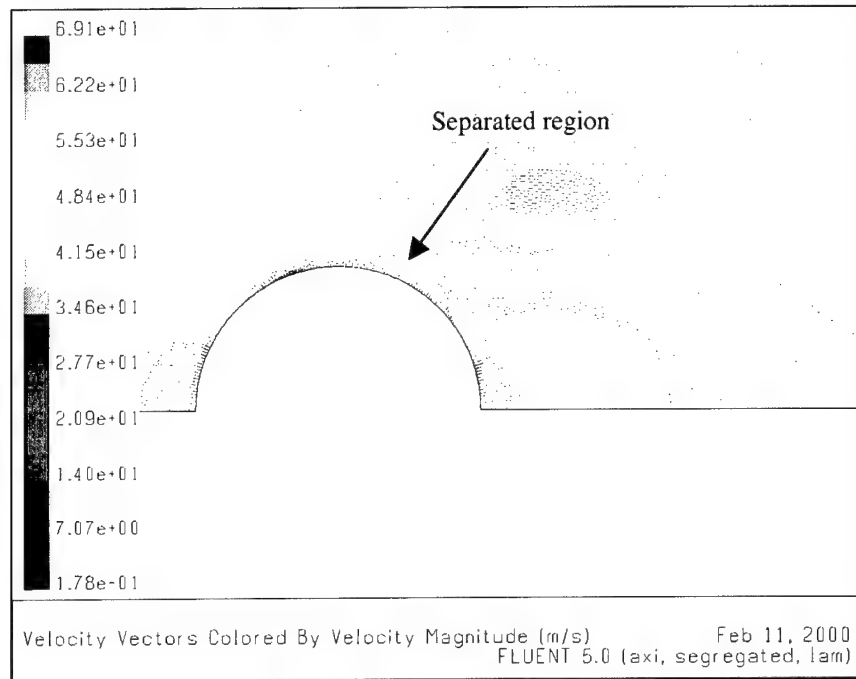


Figure 6.5. Mesh 2 axisymmetric clean sphere model separated region velocity vector plot

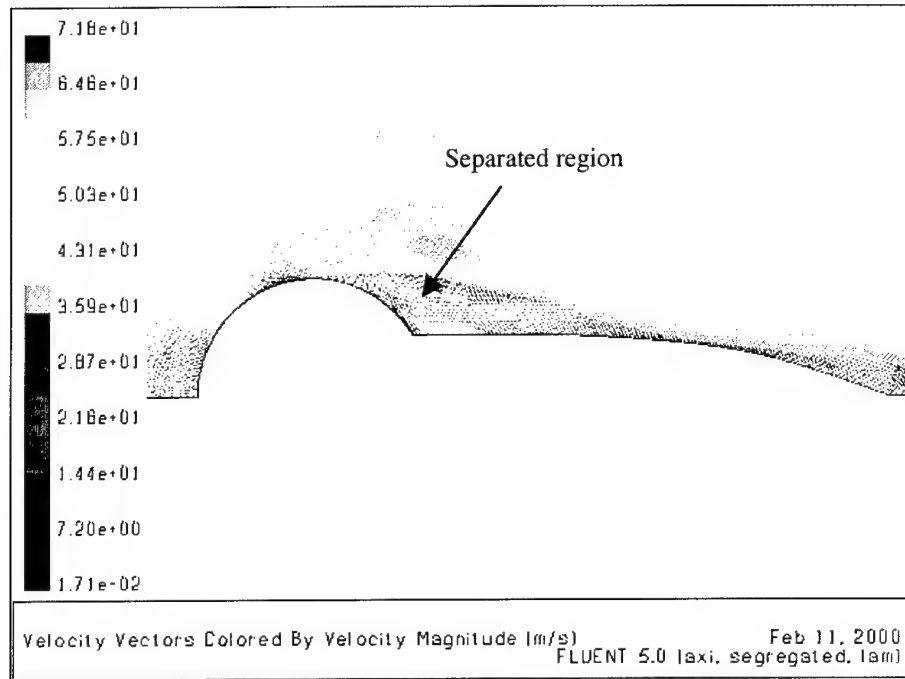


Figure 6.6. Mesh 2 axisymmetric small fairing/turret combination model separated region velocity vector plot

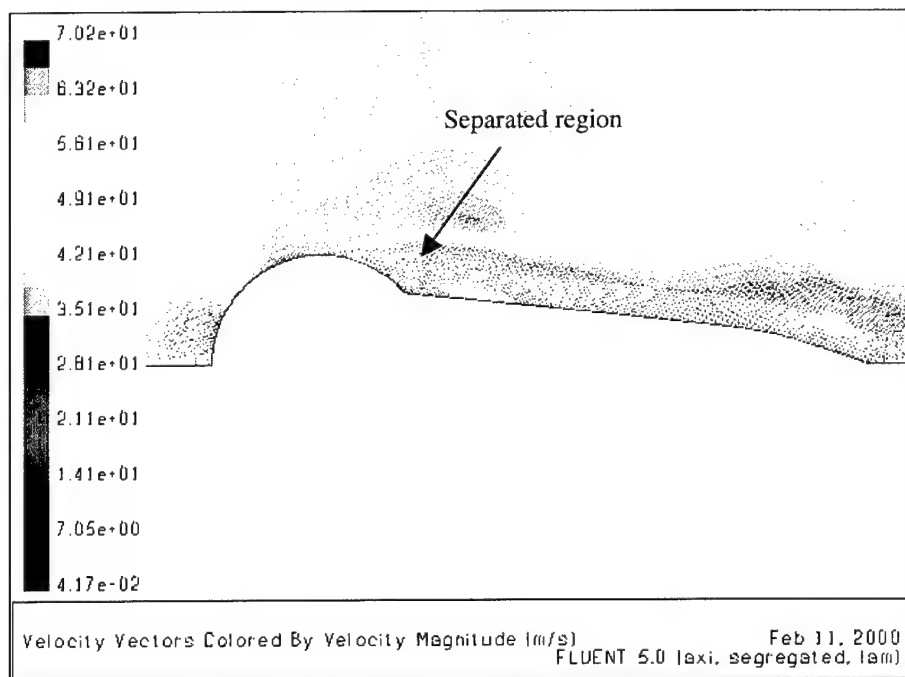


Figure 6.7. Mesh 2 axisymmetric large fairing/turret combination model separated region velocity vector plot

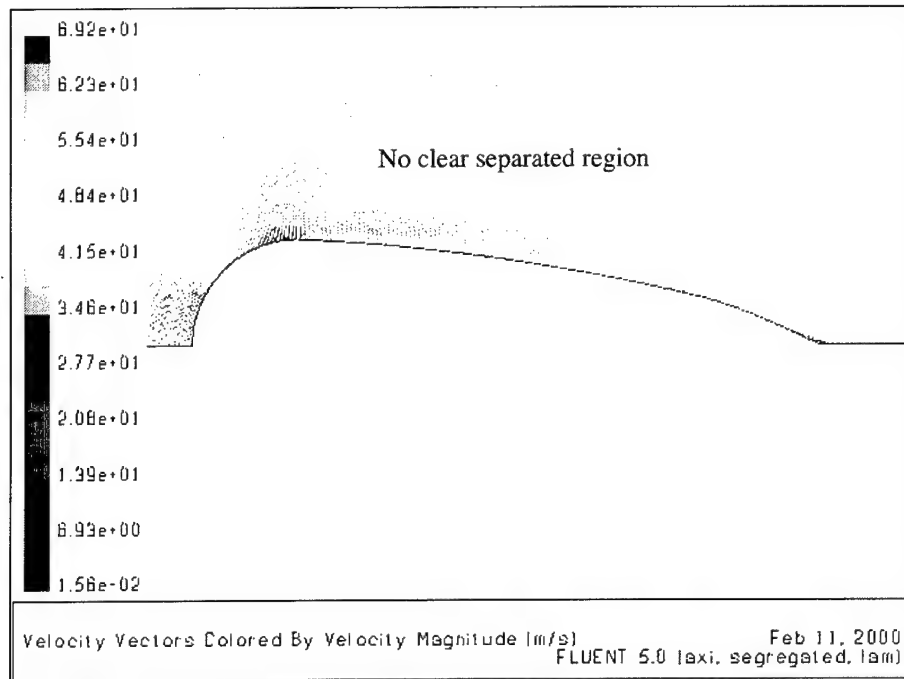


Figure 6.8. Mesh 2 axisymmetric optimized fairing/turret combination model separated region velocity vector plot

The pressure coefficient plots of the Mesh 1 and Mesh 2 geometries (Figures 6.9-6.10) provided some insight into the similar appearance of the separated regions mentioned above. The small fairing and large fairing showed relatively close agreement; both exhibited some drag-reducing pressure recovery on the aft regions of the fairing when compared to the clean turret. However, because the small and large fairings did not substantially reduce the size of the separated region (hence the similarity in C_p among the sphere, small fairing, and large fairing models), the drag reduction they provided was relatively small. Drag coefficients and associated drag reduction percentages are shown in Tables 6.6 and 6.7.

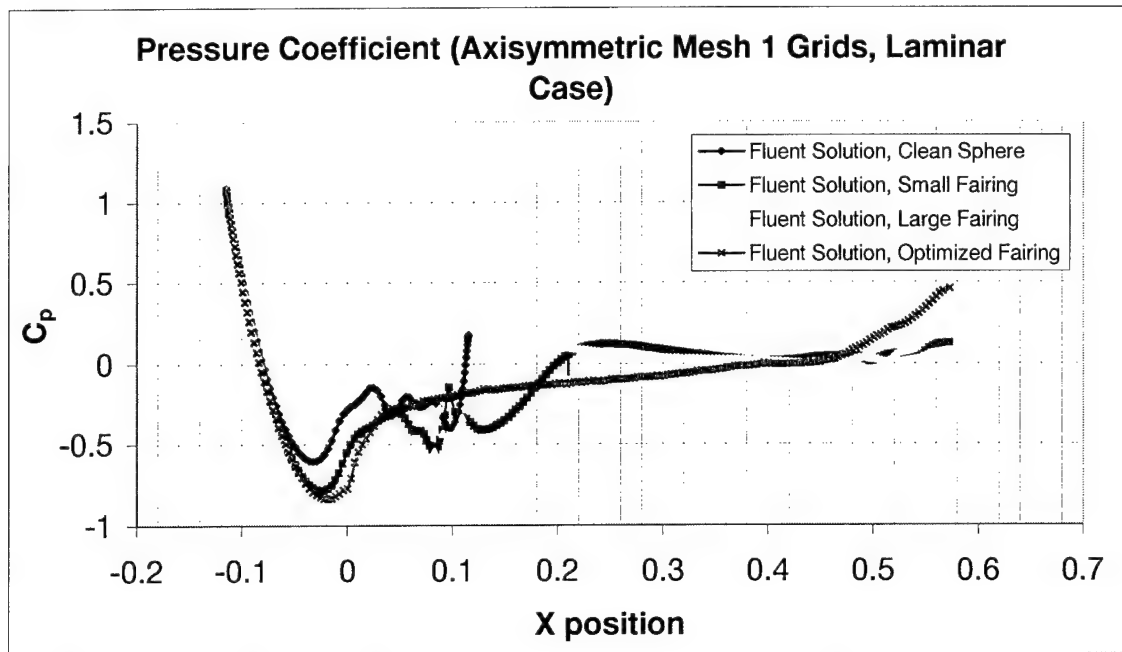


Figure 6.9. Pressure coefficient (axisymmetric Mesh 1 grids, laminar case) plots

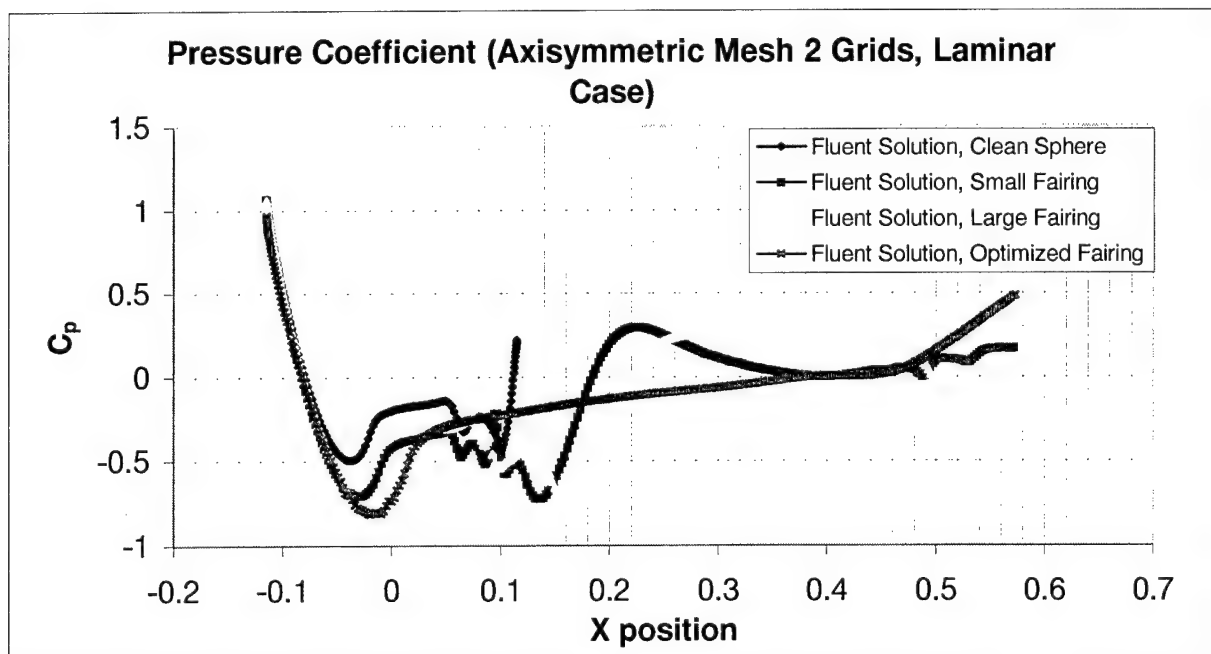


Figure 6.10. Pressure coefficient (axisymmetric Mesh 2 grids, laminar case) plots

Table 6.6. Drag coefficients for axisymmetric laminar turret/fairing combination models

	Mesh 1	Mesh 2
Clean sphere C_D	0.334	0.352
Small fairing/turret combination C_D	0.290	0.303
Large fairing/turret combination C_D	0.297	0.269
Optimized fairing/turret combination C_D	0.065	0.067

Table 6.7. Drag reduction percentages for axisymmetric laminar turret/fairing combination models compared to clean turret model

	Mesh 1	Mesh 2
Clean sphere C_D	0 %	0 %
Small fairing/turret combination C_D	13.2 %	13.9 %
Large fairing/turret combination C_D	11.1 %	23.6 %
Optimized fairing/turret combination C_D	80.5 %	81.0 %

On the other hand, the optimized fairing model all but eliminated the large separation region evident in the other models. The massive pressure recovery shown in its C_p plots explained the huge drag reduction it provided. Only upon very close inspection of the velocity vector plot can a minute separation bubble be seen (Figure 6.11). The drag coefficient associated with this model was very small compared to the clean turret configuration.

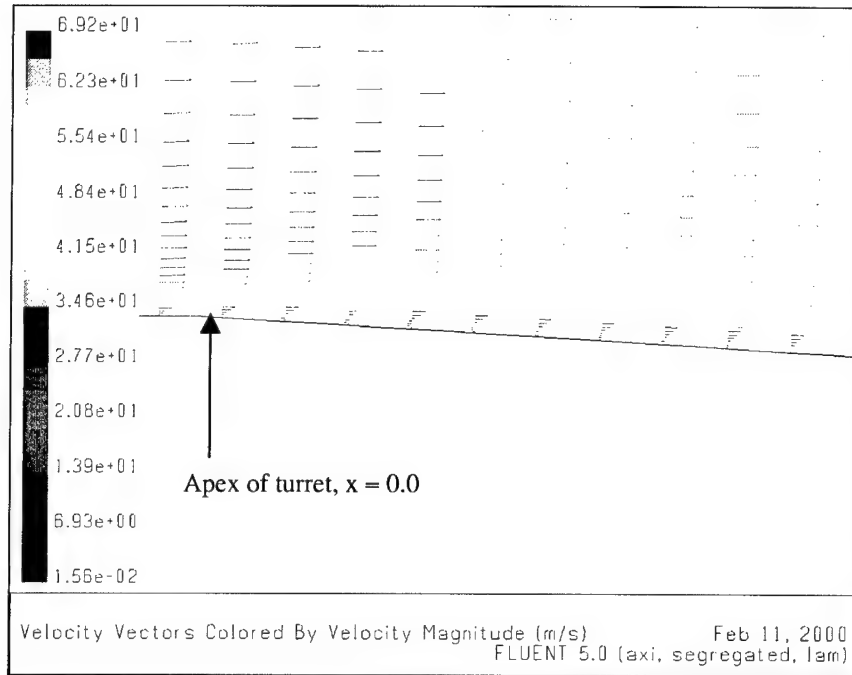


Figure 6.11. Boundary layer separation region associated with laminar axisymmetric optimized fairing/turret combination model

6.3 Axisymmetric Turbulent Turret Model Results

6.3.1 Comparison of Axisymmetric Turbulent Sphere Results to Experimental

Data

In the first part of the axisymmetric turbulent study, the results computed from the two clean turret (sphere) grids were compared to published data for transcritical flow ($Re=5.00 \times 10^6$) past a sphere and to Snyder's clean turret data. One limitation of the computational grids designed and used in this study was that they could only be classified as either fully laminar or fully turbulent; no laminar-to-turbulent flow transition modeling was possible. Although Achenbach's data was taken at a transcritical Reynolds number where the flow could be considered fully turbulent and thus could be directly compared to the turbulent computational models, Snyder's measurements were taken at a Reynolds

number in which flow transition occurred. Pressure coefficient plots for the cases mentioned above are shown in Figure 6.12. Table 6.8 shows the difference percentages in minimum computed pressure coefficient between the computed C_p plots and Achenbach's C_p plots.

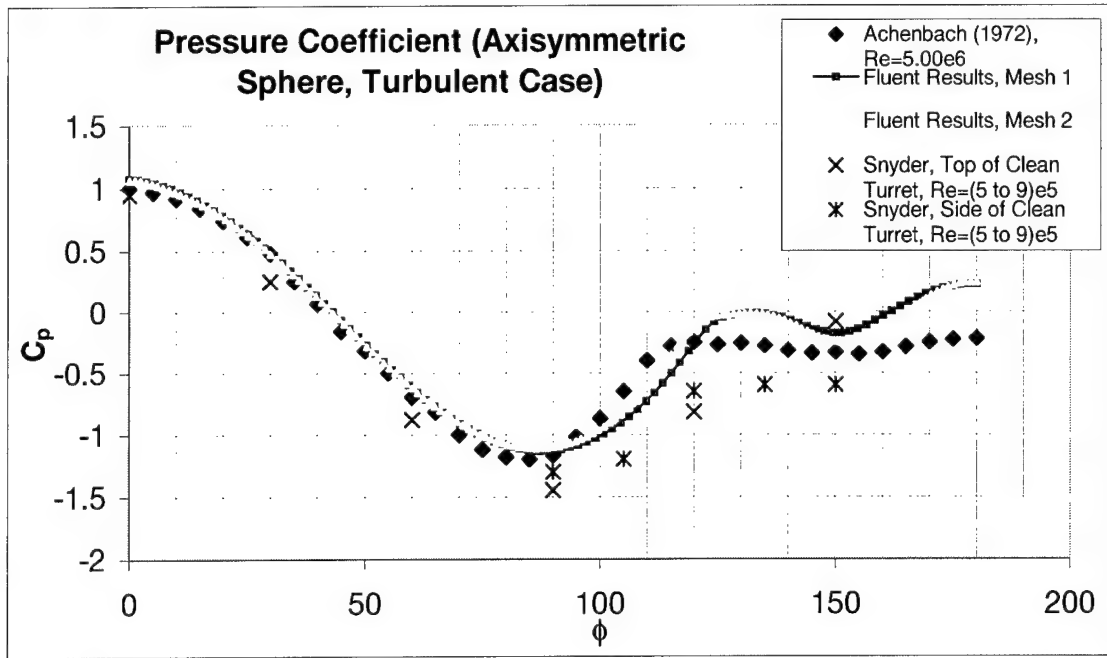


Figure 6.12. Pressure coefficient (axisymmetric sphere, turbulent case) plots

Table 6.8. Percent difference in minimum computed pressure coefficient for axisymmetric turbulent sphere cases versus Achenbach (1972)

	Mesh 1	Mesh 2
Percent difference, $C_{p \min}$	3.1 %	4.1 %

The turbulent models' pressure coefficient curves showed very good agreement with Achenbach's sphere data and Snyder's clean turret data forward of the separation point. Good agreement with Snyder's data was expected in this region since the flow over the

top of the real turret encountered the same hemispherical shape as the flow over the top of the sphere.

Figure 6.13 and Table 6.9 show the skin friction coefficient plots and difference percentages of maximum computed skin friction coefficient for each turbulent sphere grid compared to Achenbach. There was no skin friction coefficient data available from Snyder's research, although Snyder was still able to predict boundary layer separation point through the use of oil flow and tuft visualization.

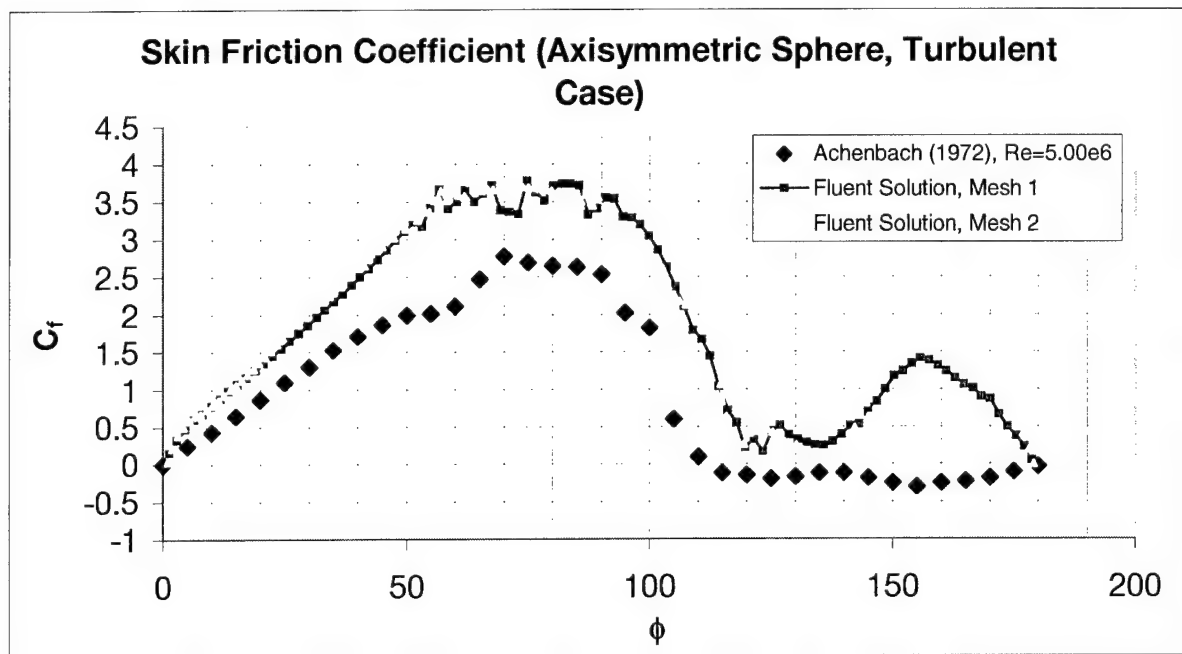


Figure 6.13. Skin friction coefficient (axisymmetric sphere, turbulent case) plots

Table 6.9. Percent difference in maximum computed skin friction coefficient for axisymmetric turbulent sphere cases versus Achenbach (1972)

	Mesh 1	Mesh 2
Percent difference, $C_{f, max}$	32.5 %	35.0 %

Like the laminar axisymmetric sphere cases, it was again difficult to draw accurate conclusions about the accuracy of the skin friction coefficient values computed numerically aft of the separation point since FLUENT 5 only plots the absolute value of C_f . However, unlike the laminar cases, the computed skin friction coefficient curves did not track well with Achenbach's data forward of the separation point. The general trends of the curves were the same though, which helped to provide a possible explanation for the differences between the experimental and numerical C_f values. The accuracy of skin friction coefficient prediction in numerical simulations is highly dependent on the accurate resolution of the turbulent boundary layer near the surface of the body. Accurate calculation of near-wall effects requires an extremely fine mesh in that region. Although the Spalart-Allmaras turbulence model accurately predicted the boundary layer separation points (as will be shown), it was designed for success in relatively crude turbulent simulations on course meshes (such as those used in this study). Thus, although the bulk turbulent effects were well represented, effects that required especially fine mesh resolution (such as skin friction coefficient calculation) might not have been as accurately calculated. Plus, since boundary layer separation arises due to pressure variations, accurate separation point predictions are dependent on accurate pressure calculations, which require a less fine mesh than do skin friction calculations. Because of this, it is entirely possible that numerical separation point predictions are accurate whereas skin

friction calculations are not. However, the discrepancies between actual and computed C_f curves were not expected to greatly affect the reliability of the total drag prediction since skin friction drag only accounted for 10 to 20 percent of the total drag in these cases. Again, as in the axisymmetric sphere cases, the C_p and C_f plots indicate that grid independence was achieved since differences in grid resolution did not affect the accuracy of the results to a significant degree.

Table 6.10 shows the separation points associated with the skin friction coefficient plots as well as the difference percentages between the computed separation points and Achenbach's experimental separation point. This table also shows the separation point along the top of the clean turret as reported by Snyder. Clearly, the position of the separation point predicted in Snyder's experiments indicate that the turret was operating in the turbulent flow regime. Comparisons between the numerically predicted separation angle and Snyder's separation angle data were possible due to the spherical shape of the real turret on its top and sides.

Table 6.10. Separation points in degrees and difference percentages for axisymmetric turbulent sphere cases

	Achenbach (1972)	Mesh 1	Mesh 2	Snyder (1998), sides, +/- 5	Snyder (1998), top, +/- 5
Separation point (degrees)	118	122.6	118.6	125	125
Percent difference	n/a	3.9 %	0.5 %	n/a	n/a

As with the laminar cases, the numerical separation point predictions matched Achenbach's experimental data extremely closely. In addition, the numerical models matched the separation point that Snyder measured on the top of the clean turret very well. Because of the tuft method that Snyder used to predict the separation point, it is possible that separation in his experiments occurred earlier than he was able to measure; in other words, because of the size and weight of the tufts, the separation region would have to grow somewhat before the tufts would be able to detect its presence. Close agreement between Snyder's results and the numerical data was expected since flow over the top of Snyder's turret model encountered the same shape as flow over a sphere encounters.

Table 6.11 shows the drag coefficients measured for Achenbach's transcritical turbulent sphere study, for the two turbulent clean sphere numerical models, and for Snyder's clean turret. Difference percentages between the numerical data and Achenbach's turbulent sphere drag measurement are also included.

Table 6.11. Drag coefficients and difference percentages for axisymmetric turbulent sphere cases

	Achenbach (1972)	Mesh 1	Mesh 2	Snyder (1998)
Drag coefficient, C_D	0.19	0.17	0.16	0.57
Percent difference	n/a	10.5 %	15.8 %	n/a

Although the drag coefficient chosen for comparison was at the maximum Reynolds number Achenbach investigated (to most closely match the conditions of the fully turbulent numerical model), the drag coefficients Achenbach measured in the supercritical to transcritical Reynolds number range varied from 0.09 to 0.19 as Reynolds number varied from 4×10^5 to 5×10^6 . This implies that drag is Reynolds number-dependent in the supercritical to transcritical Reynolds number range, and that the small mismatch between Achenbach's drag coefficient and the numerically computed drag coefficients may be due to Reynolds number mismatch more than inaccuracies in the numerical method. Achenbach also presents other drag coefficient results in his paper that were obtained through integration rather than direct measurement; those results predict an even larger range of drag coefficient variation (from 0.07 to 0.24 over the same Re range). Further, the pressure coefficient plots show that more pressure recovery occurred on the aft region of the sphere for the two numerical models than that which occurred on Achenbach's sphere. The higher pressure recovery evident on the numerical sphere models explains the reduced drag coefficients they predicted when compared to Achenbach's data. Differences between Snyder's clean turret drag coefficient and the drag coefficients predicted by the numerical models are primarily due to differences in geometry. The actual physical turret model was comprised of a cylinder blended to a sphere and was mounted flush to a wall, whereas the numerical clean turret models were simply free-floating axisymmetric spheres. The flow over the spheres received pressure relief from all sides. For the turret attached to a wall, the base of the separation region behind the turret extended downward to the wall. This low-pressure wake would be

much larger than the corresponding wake behind the clean sphere, and this would result in an increase in pressure drag.

6.3.2 Effects of Aft-Mounted Fairings on Drag Reduction in Turbulent Flow Field

Figure 6.14 shows the skin friction coefficient plots for all four Mesh 1 numerical models, and Figure 6.15 shows the skin friction coefficient plots for the three converged Mesh 2 numerical models (the Mesh 2 optimized fairing simulation generated a diverged solution). Table 6.12 shows the associated separation points for all of the Mesh 1 and Mesh 2 geometries as well as the separation points that Snyder observed on the actual fairing/turret models.

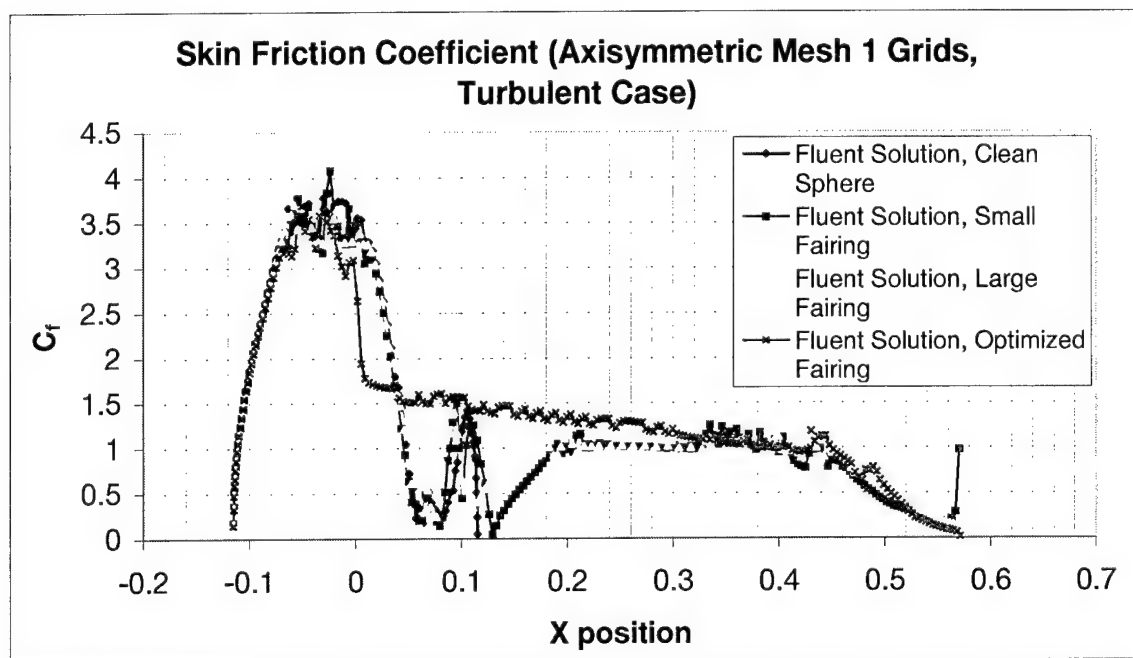


Figure 6.14. Skin friction coefficient (axisymmetric Mesh 1 grids, turbulent case) plots

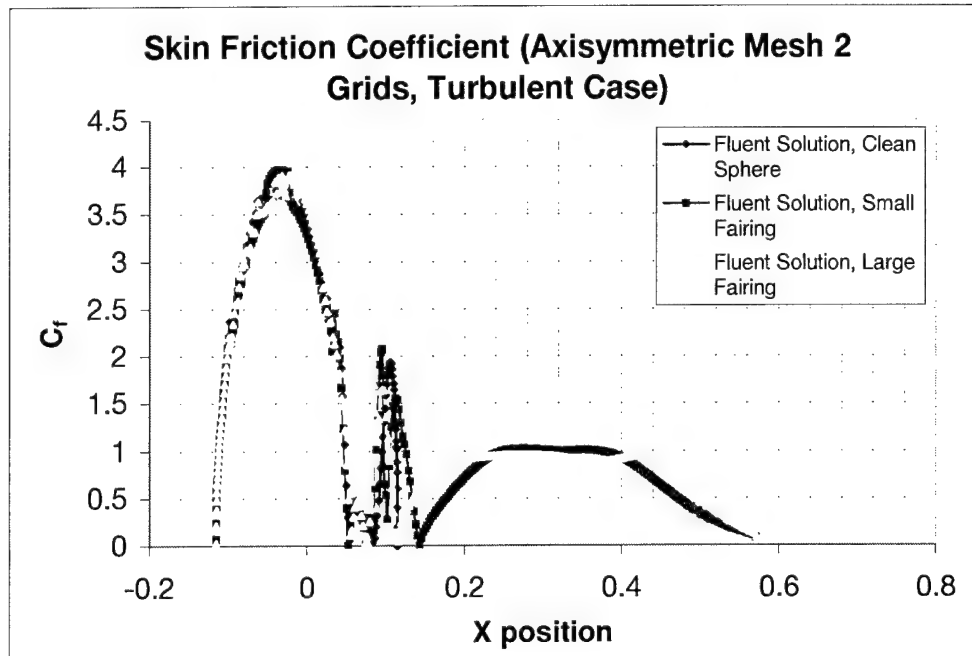


Figure 6.15. Skin friction coefficient (axisymmetric Mesh 2 grids, turbulent case) plots

Table 6.12. Separation points in degrees for all axisymmetric turbulent grids

	Mesh 1	Mesh 2	Snyder (1998), side, +/- 5	Snyder (1998), top, +/- 5
Clean sphere separation point (degrees)	123	119	125	125
Small fairing separation point (degrees)	126	116	125	125
Large fairing separation point (degrees)	126	119	135	135
Optimized fairing separation point (degrees)	none	diverged	n/a	n/a

The separation point data extrapolated from the C_f plots shows that like the laminar computations, all of the axisymmetric turbulent numerical models, regardless of fairing

configuration, predict very similar boundary layer separation locations. The numerical models also agree well with Snyder's separation point visual estimates. As expected, the turbulent separation points moved aft compared to the laminar separation points predicted using the same grids. The velocity vector plots of the domains of the Mesh 1 models (Figures 6.16-6.19) bear this fact out and also reveal that the wakes associated with the turbulent models are much smaller than those evident in the laminar models. Mesh 2 velocity vector plots are displayed because of their higher resolution. A Mesh 1 velocity vector plot is shown for the optimized fairing/turret combination case because no corresponding Mesh 2 plot was available.

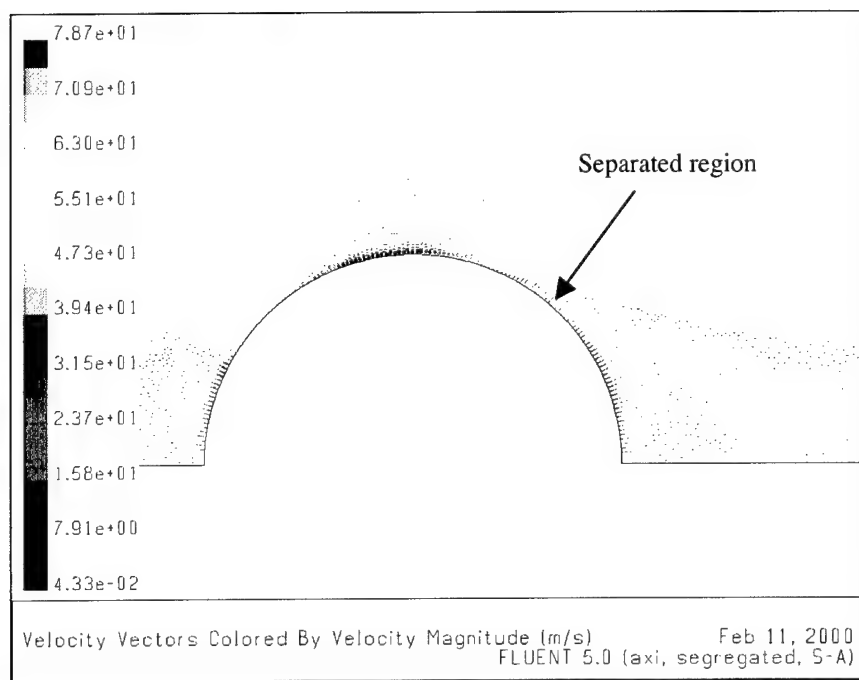


Figure 6.16. Mesh 2 axisymmetric turbulent clean sphere model separated region velocity vector plot

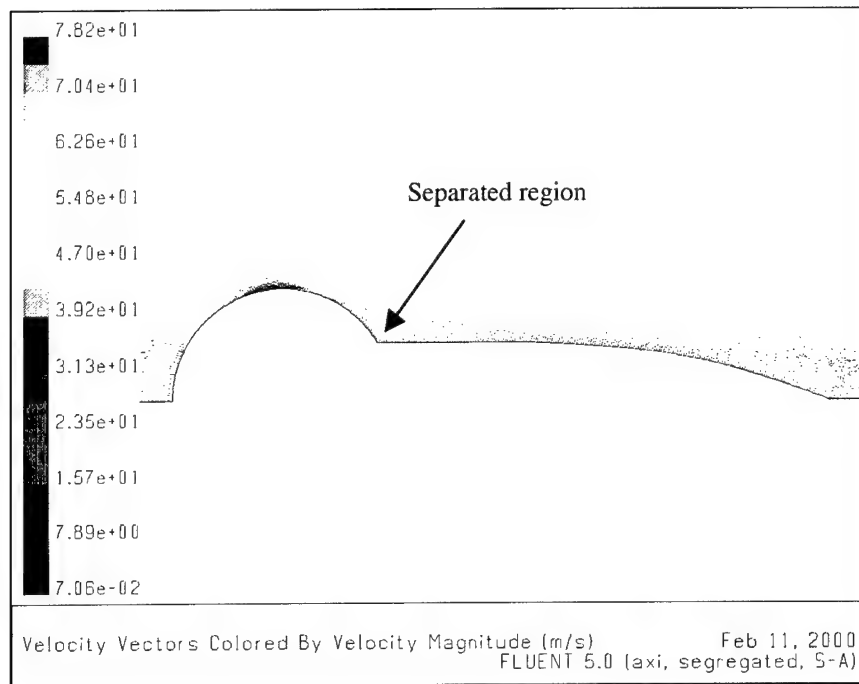


Figure 6.17. Mesh 2 axisymmetric turbulent small fairing/turret combination model separated region velocity vector plot

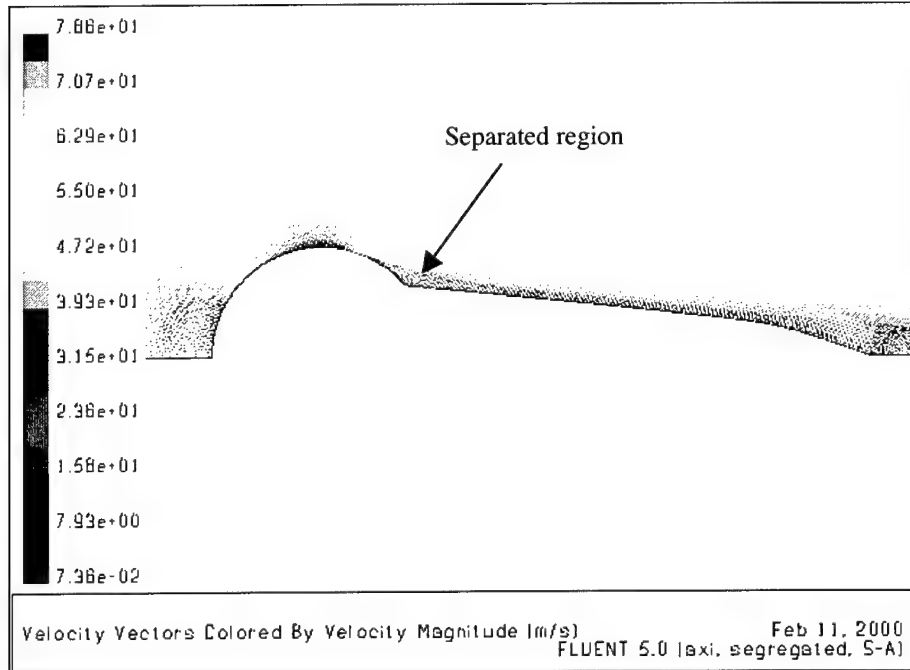


Figure 6.18. Mesh 2 axisymmetric turbulent large fairing/turret combination model separated region velocity vector plot

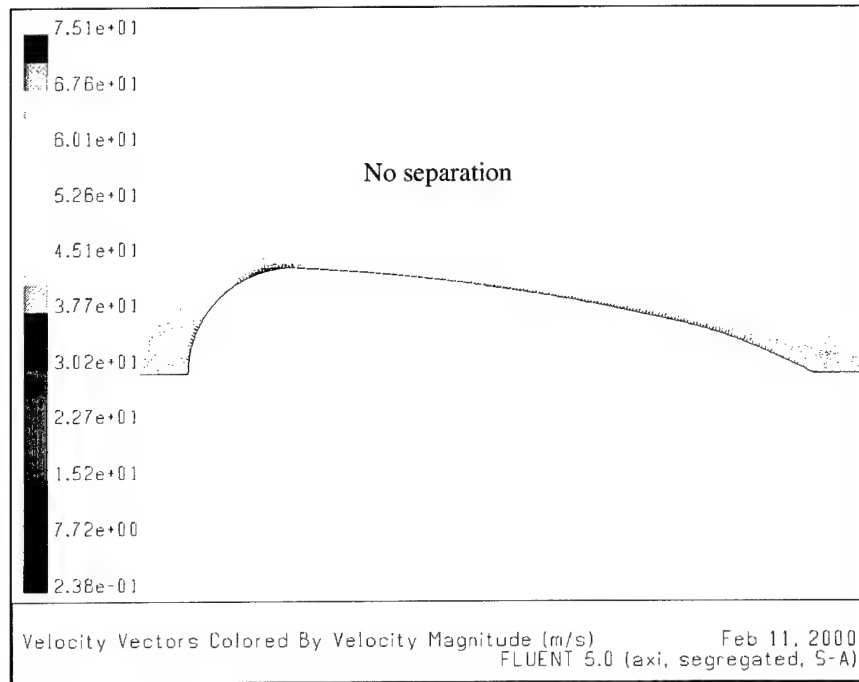


Figure 6.19. Mesh 1 axisymmetric turbulent optimized fairing/turret combination model velocity vector plot

A difference between the small and large numerical fairing configurations' drag coefficients was more evident in the turbulent results than it was in the laminar cases. The most likely explanation for this phenomenon is the smaller low-pressure wakes experienced in the turbulent flow fields. This, coupled with the fact that the turbulent flow was more likely to reattach than the laminar flow, meant that the large fairing was better able to reduce the size of the separated region than was the small fairing. This phenomenon is clearly visible in Figures 6.17 and 6.18 where it can be seen that the large fairing/turret configuration had a noticeably smaller low-pressure wake than did the small fairing/turret configuration. This flow feature was also resolved in the skin friction coefficient plots. The second hump seen in these plots (which should be negative) indicates the region of recirculating, separated flow. It is apparent that this region was smaller for the large fairing configuration than for the small fairing configuration.

Further, the optimized fairing geometry (Figure 6.19) has completely eliminated boundary layer separation, generating a massive pressure drag reduction – double that created by the large fairing/turret configuration. Numerically-predicted drag coefficients, drag coefficients from Snyder’s data, and associated drag reduction percentages for all turret/fairing combinations are shown in Table 6.13.

Table 6.13. Numerical and experimental drag coefficients and drag reduction percentages for all turret/fairing combinations

	Mesh 1	Mesh 2	Snyder (1998)
Clean turret C_D	0.171	0.157	0.57
Small fairing/turret combination C_D	0.153	0.142	0.29
Large fairing/turret combination C_D	0.124	0.108	0.26
Optimized fairing/turret C_D	0.0797	n/a	n/a
Small fairing drag reduction	10.5 %	9.6 %	49.1 %
Large fairing drag reduction	27.5 %	31.2 %	54.4 %
Optimized fairing drag reduction	54.4 %	n/a	n/a

The results discussed above are further borne out by the pressure coefficient data shown in Figures 6.20 and 6.21. A substantial pressure recovery region is shown for both small and large fairing configurations immediately after the reversed flow region discussed earlier; this higher-pressure area corresponds to the reattachment of the boundary layer and would lead to pressure drag reduction.

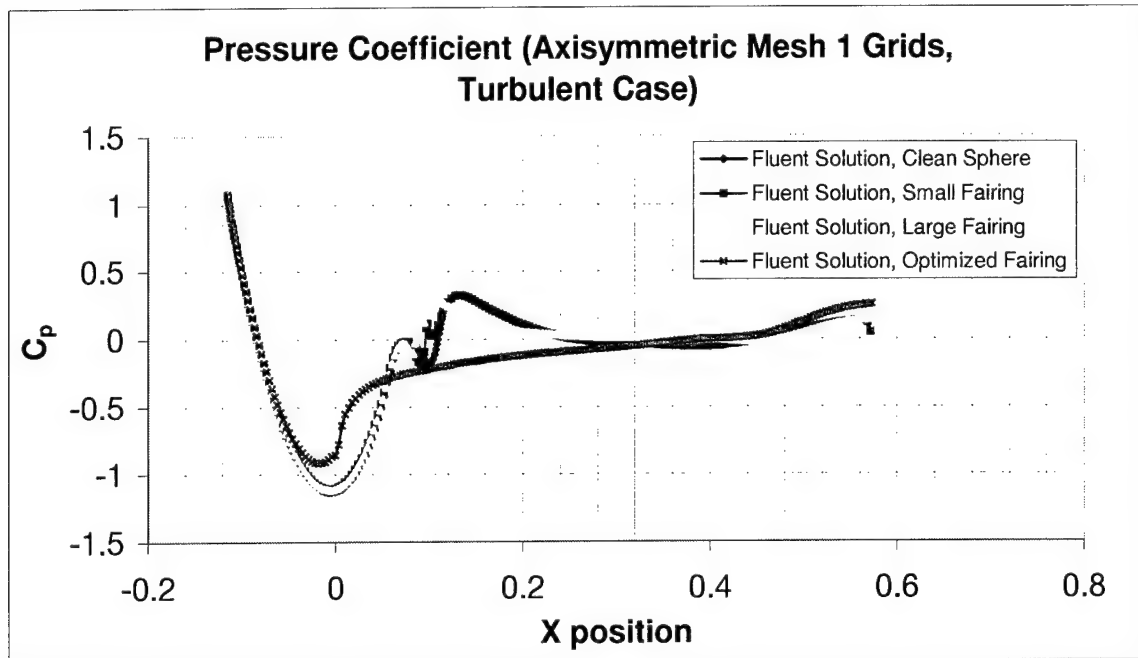


Figure 6.20. Pressure coefficient (axisymmetric Mesh 1 grids, turbulent case) plots

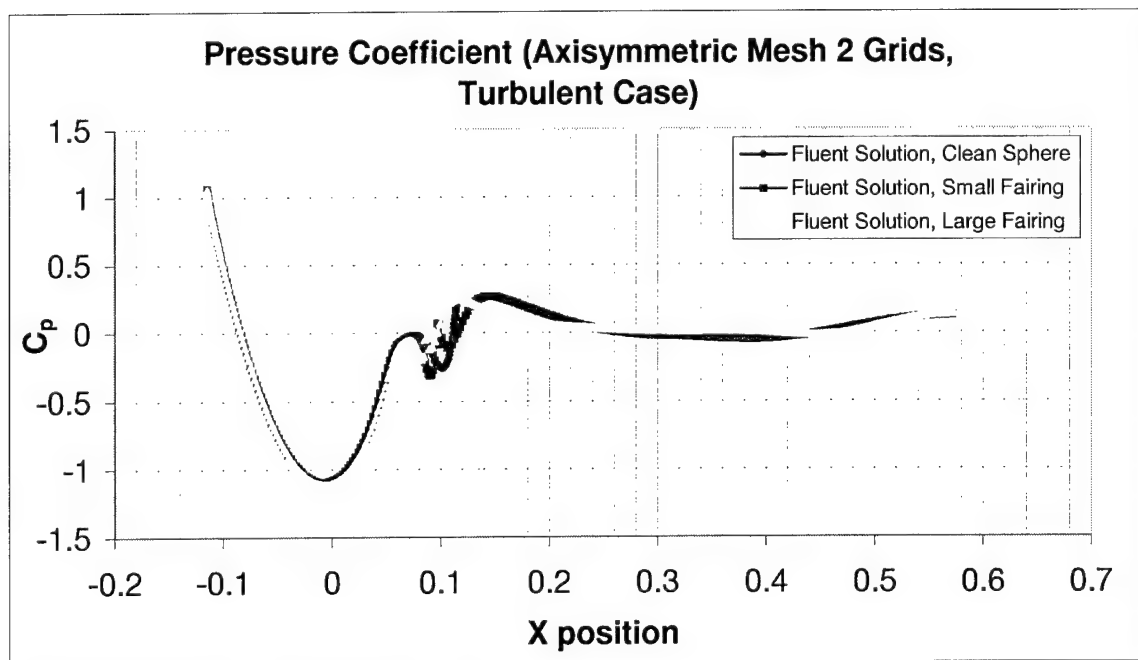


Figure 6.21. Pressure coefficient (axisymmetric Mesh 2 grids, turbulent case) plots

Although the numerical C_p data for the small and large fairing/turret combinations follow Snyder's experimental pressure coefficient data rather closely (Figures 6.22 and 6.23), there still exists a large difference in both the predicted drag coefficients and associated drag reduction percentages between the experimental and numerical studies. This is due to the difference in geometries between the numerical models and Snyder's physical models. Although both the numerical and experimental results describe increasing drag reduction with increasing fairing size, the physical models predict a much larger drag reduction for the small and large fairings than do the numerical models. As described before, Snyder's clean turret had a larger drag coefficient than did numerical clean sphere due to the turret's larger low-pressure wake. Since Snyder's fairings extended all the way to the wall, as did his turret, his fairings were able to reduce or eliminate a larger percentage of the separation region than were the axisymmetric fairings, leading to a larger percentage of drag reduction.

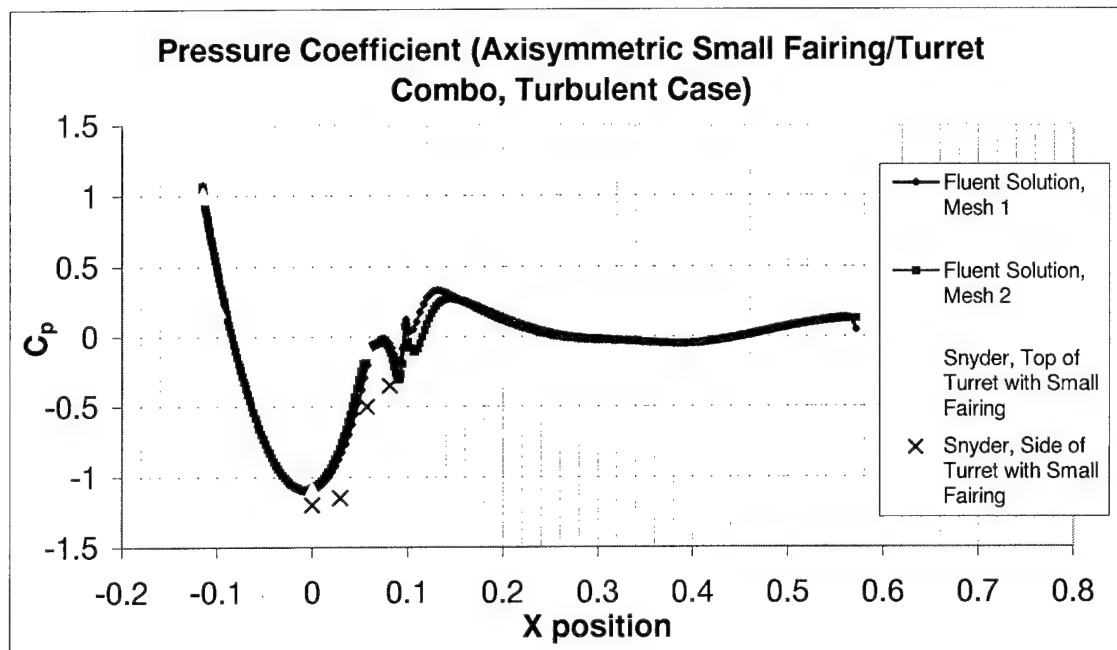


Figure 6.22. Pressure coefficient (axisymmetric small fairing/turret combo, turbulent case) plots

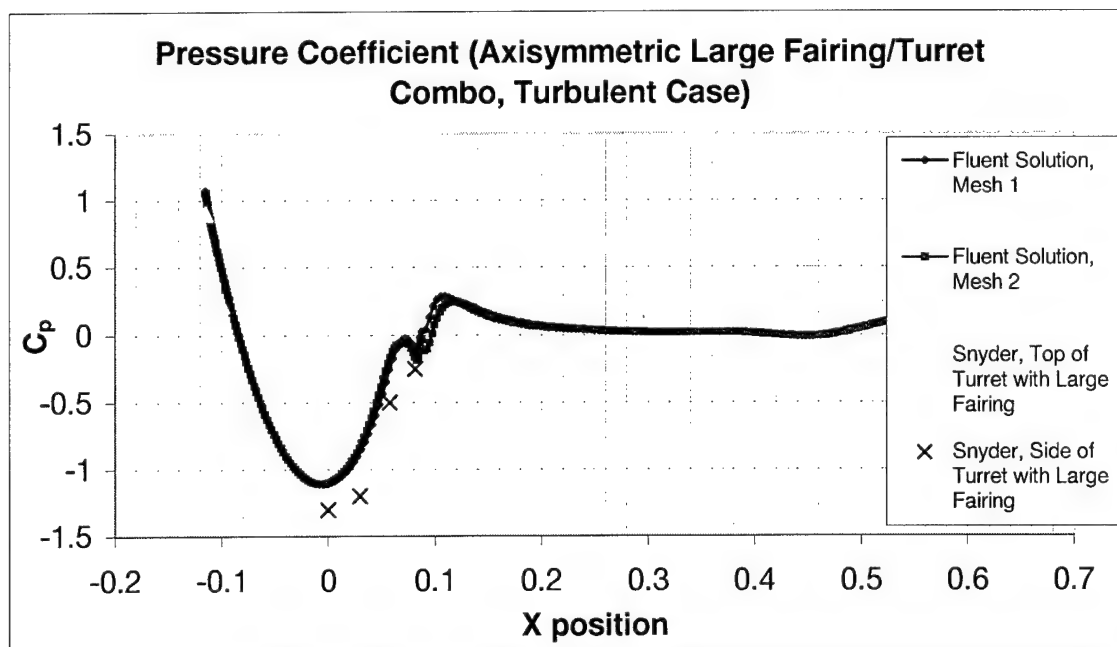


Figure 6.23. Pressure coefficient (axisymmetric large fairing/turret combo, turbulent case) plots

Chapter 7 – Conclusions and Recommendations

There were three objectives of this study. First, the CFD technique was validated by solving the flow field around laminar and turbulent axisymmetric sphere models. Second, the flow was modeled and the drag coefficients were computed in both laminar and turbulent modes for axisymmetric turret/fairing models that closely matched physical models used in previous research. Finally, an optimized fairing configuration was designed and numerically tested, demonstrating the suitability of CFD to design optimization.

Numerical data for the axisymmetric sphere CFD models showed good agreement with experimental data, particularly in predicted boundary layer separation point and for skin friction coefficient and pressure coefficient values on the leading surfaces of each geometry. With the laminar sphere models, the maximum difference between the numerical and experimental data was 3.6 percent for minimum pressure coefficient, 7.8 percent for maximum skin friction coefficient, and 2.4 percent for separation point. The turbulent sphere models produced maximum differences of 4.1 percent for the minimum pressure coefficient when compared to historical data, 35 percent for maximum skin friction coefficient, and 3.9 percent for separation point. Possible explanations for differences between computed and experimental C_f data were discrepancies in the turbulence model and to lack of mesh refinement in the boundary layer. However, these discrepancies were not expected to have a significant impact on drag coefficient prediction. For example, the numerically computed maximum skin friction coefficient

was greater than the experimentally measured one, although the numerically computed drag coefficient was less than the experimentally measured one. The maximum difference between numerical and experimental drag coefficients in the turbulent regime was 15.8 percent; this difference was felt to be due to Reynolds number mismatch and not imprecision in the numerical model.

Laminar axisymmetric turret/fairing CFD models were used to demonstrate the effectiveness of CFD in predicting drag reduction of aft-mounted fairings in purely laminar flow. The fairings did produce a measurable amount of drag reduction as reported in Section 6.3.2. However, due to the relatively early separation points of the laminar flows and the similarities in the low-pressure wakes between the clean turret and fairing-equipped turret configurations as shown in velocity vector plots, the fairings were unable to provide the same level of drag reduction in the laminar studies as they did in the turbulent studies.

Turbulent axisymmetric turret/fairing CFD model data was directly compared to the experimental results documented in Snyder's work. Good agreement was shown between the separation points noted in the physical experiments and those predicted by the numerical models; maximum differences were on the order of 10 percent. Good agreement was also shown between the numerical pressure coefficient data although experimental data was only available over a limited part of the surface of the turret/fairing models. Similar trends in drag reduction were also noted between the experimental and numerical studies – as fairing size increased, drag decreased. This

effect was readily observable as a reduction in size of low-pressure wakes visible in velocity vector plots. However, due to the differences in geometry (and the low-pressure wakes associated with these differences), the small and large fairings were more effective in reducing the drag effects of the low-pressure wake for the experimental models than they were in the axisymmetric numerical models. Despite these differences in drag coefficient, the computational models were quite useful in trend prediction and geometry optimization.

The optimized fairing design produced a tremendous drag reduction when compared to the clean turret numerical models. An 81 percent drag reduction was realized with the laminar models and a 54 percent drag reduction was realized with the turbulent model when compared to numerical clean turret data. The optimized turbulent fairing geometry predicted double the drag reduction of the large turbulent fairing geometry. These significant drag reductions were due to the virtual elimination of boundary layer separation; the pressure drag-producing low-pressure wake simply did not exist. Unfortunately, this improvement in drag reduction comes at the expense of a reduced viewing area for the laser turret.

In summary, the objectives of this study were met. The CFD models showed good agreement with the published data for both laminar and turbulent sphere models, particularly forward of the boundary layer separation point. The turret/fairing CFD models accurately modeled the trends shown in the Snyder's experimental work; discrepancies noted were largely due to geometry differences. Finally, CFD was shown

to be a valuable tool in design optimization; the optimized fairing design showed a significant drag reduction when compared to the other CFD fairing/turret models.

Recommendations for further study in this area include:

1. Increase the Reynolds number at which the numerical simulations were performed. As noted by Snyder, this study is only valid for the low speed portions of the flight regime. By increasing the speed of the flow, compressibility effects would become pronounced and the effectiveness of the passive drag reduction devices at higher speeds could be tested. Of particular interest would be these devices' performance at or near the critical Mach number, where shocks begin to form and drag increases sharply. Since the critical Mach number for a sphere is 0.57 (Shapiro, 1953), the real turret would almost certainly see sonic flow over it at some point during its flight. The ability to easily vary Mach number and Reynolds number in CFD simulations would prove extremely valuable for future simulations that cover the entire flight envelope of the turret.
2. Design and test fully three-dimensional computational models. Although the computer platform used for this work was not able to provide the power needed to solve 3D models with sufficient resolution, this change would significantly enhance the validity of the results. Out-of-plane fluid motion and interaction could be studied and data taken from 3D simulations could be compared directly to experimental data with little or no ambiguity. Most significantly, Snyder's geometry could be exactly duplicated and tested.

3. Employ a more concentrated boundary layer mesh and/or a more accurate turbulence model. Though this change might affect the computational efficiency of the model, it could help to better resolve flow parameters inside the low-pressure wake and near the body surface.
4. Model the laminar-to-turbulent flow transition. This would require re-building the grids used in this study by dividing the domain into laminar and turbulent regions. This enhancement would allow for more accurate Reynolds number matching and better flow property prediction.

Bibliography

- Achenbach, Elmar. "Experiments on the flow past spheres at very high Reynolds numbers." Journal of Fluid Mechanics 54.3 (1972): 565-575.
- Anderson, John D., Jr. Computational Fluid Dynamics – The Basics With Applications. New York: McGraw-Hill, 1995.
- Anderson, John D., Jr. Introduction to Flight (Third Edition). New York: McGraw-Hill, 1989.
- Anderson, John D., Jr. Fundamentals of Aerodynamics (Second Edition). New York: McGraw-Hill, 1991.
- Fluent Incorporated. FLUENT 5 User's Guide. 4 vols. Lebanon NH: published by author, 1998.
- Fluent Incorporated. GAMBIT I Modeling Guide. Lebanon NH: published by author, 1998.
- Fluent Incorporated. GAMBIT I User's Guide. Lebanon NH: published by author, 1998.
- Hoerner, Sigward F. Fluid-Dynamic Drag. Midland Park NJ: published by author, 1965.
- Hoffmann, Klaus A. and Steve T. Chiang. Computational Fluid Dynamics (Third Edition). 2 vols. Wichita KS: Engineering Educational System, 1998.
- Shapiro, A. H. The Dynamics and Thermodynamics of Compressible Fluid Flow. New York: Ronald, 1953.
- Snyder, Christopher H. Wind Tunnel Testing For Drag Reduction of an Aircraft Laser Turret. MS thesis, AFIT/GAE/ENY/98J-02. School of Aeronautical Engineering, Air Force Institute of Technology (AU), Wright-Patterson AFB OH, June 1998.
- Tannehill, John C., Dale A. Anderson and Richard H. Pletcher. Computational Fluid Mechanics and Heat Transfer (Second Edition). Washington DC: Taylor & Francis, 1997.
- Walterick, Ronald E. and James T. Van Kuren. Wind Tunnel Tests of Fairings for an On-Gimbal Telescope Turret. Technical memorandum, AFFDL-TM-75-177 FXM. Analysis Group, Aeromechanics Division, AF Flight Dynamics Laboratory, Wright-Patterson AFB OH, November 1975.

Vita

Captain Gregory J. Schwabacher was born in Camp Springs, Maryland on December 25, 1972. He graduated from the Thomas Jefferson High School for Science and Technology in Alexandria, Virginia in 1990 and subsequently attended the University of Virginia in Charlottesville, Virginia. He graduated with a Bachelor of Science degree in Aerospace Engineering in 1994 and received a reserve commission as a Second Lieutenant in the United States Air Force through the Reserve Officer Training Corps (ROTC). His first assignment was to the Aircraft Maintenance Officer Course at Sheppard Air Force Base, Texas in September 1994. After his graduation from technical training, he was stationed at Eglin Air Force Base as an aircraft maintenance officer. In 1998 he was assigned to Wright-Patterson Air Force Base Ohio where he studied Aeronautical Engineering as a resident student at the Air Force Institute of Technology. He is married to the former Kelly Kirby of Springfield, Virginia.

REPORT DOCUMENTATION PAGE			Form Approved OMB No. 0704-0188	
Public reporting burden for this collection of information is estimated to average 1 hour per response, including the time for reviewing instructions, searching existing data sources, gathering and maintaining the data needed, and completing and reviewing the collection of information. Send comments regarding this burden estimate or any other aspect of this collection of information, including suggestions for reducing this burden, to Washington Headquarters Services, Directorate for Information Operations and Reports, 1215 Jefferson Davis Highway, Suite 1204, Arlington, VA 22202-4302, and to the Office of Management and Budget, Paperwork Reduction Project (0704-0188), Washington, DC 20503.				
1. AGENCY USE ONLY (Leave blank)		2. REPORT DATE May 2000		3. REPORT TYPE AND DATES COVERED Master's Thesis
4. TITLE AND SUBTITLE COMPUTATIONAL FLUID DYNAMICS TESTING FOR DRAG REDUCTION OF AN AIRCRAFT LASER TURRET			5. FUNDING NUMBERS	
6. AUTHOR(S) Gregory J. Schwabacher, Capt, USAF				
7. PERFORMING ORGANIZATION NAME(S) AND ADDRESS(ES) Air Force Institute of Technology 2750 P Street WPAFB OH 45433-7765			8. PERFORMING ORGANIZATION REPORT NUMBER AFIT/GAE/ENY/00M-11	
9. SPONSORING/MONITORING AGENCY NAME(S) AND ADDRESS(ES) Mr. Marc Masquelier (937) 255-4174 AFRL/SN 2241 Avionics Circle WPAFB OH 45433-7303			10. SPONSORING/MONITORING AGENCY REPORT NUMBER	
11. SUPPLEMENTARY NOTES Advisor: Maj Jeffrey Bons jeffrey.bons@afit.af.mil (937) 255-3636 x4643				
12a. DISTRIBUTION AVAILABILITY STATEMENT Approved for public release; distribution unlimited			12b. DISTRIBUTION CODE	
13. ABSTRACT (Maximum 200 words) A computational study was conducted on the use of aft-mounted fairings for passive drag reduction on a sphere at $Re=866,000$. The sphere dimensions and operating Reynolds number were selected to approximate the flow around a proposed aircraft laser turret for which experimental data was available. To establish the validity of the computational model, flow predictions were compared to sphere data available in the open literature. The model, exercised in both the laminar and turbulent modes, showed good agreement with the published data. Two proposed laser turret fairings were then evaluated computationally: a large fairing (beginning at 49.5 degrees past the sphere apex) and a small fairing (beginning at 58.95 degrees past the sphere apex). Existing wind tunnel models were used to generate axisymmetric computational grids that approximated the geometry of these models. The computed flow field and associated drag reduction were comparable to the experimental results obtained from the wind tunnel testing. Differences in drag from the model to the experiment were explained by the axisymmetric simplifications made in the model. Finally, a new, optimized fairing model was designed which eliminated the separation zone on the aft portion of the sphere. The optimized model predicted double the drag reduction compared to the large fairing computational model.				
14. SUBJECT TERMS Turret, Fairing, Drag Reduction, Pressure Drag, Separation, CFD, Computational Fluid Dynamics, Sphere, Axisymmetric			15. NUMBER OF PAGES 114	
			16. PRICE CODE	
17. SECURITY CLASSIFICATION OF REPORT UNCLASSIFIED	18. SECURITY CLASSIFICATION OF THIS PAGE UNCLASSIFIED	19. SECURITY CLASSIFICATION OF ABSTRACT UNCLASSIFIED	20. LIMITATION OF ABSTRACT UL	